Mon. Not. R. Astron. Soc. **000**, 000–000 (0000) Printed 26 June 2012 (MN LATEX style file v2.2)

The Phoenix Project: the Dark Side of Rich Galaxy Clusters

L. Gao[1,2⋆], J. F. Navarro[3], C. S. Frenk[2], A. Jenkins[2], V. Springel[4,5], S. D. M. White[6]
[1]*Partner Group of the Max Planck Institute for Astrophysics, National Astronomical Observatories, Chinese Academy of Sciences, Beijing, 100012, China*
[2]*Institute of Computational Cosmology, Department of Physics, University of Durham,Science Laboratories, South Road, Durham DH1 3LE*
[3]*Department of Physics and Astronomy, University of Victoria, PO Box 3055 STN CSC, Victoria, BC, V8W 3P6 Canada*
[4]*Heidelberger Institut für Theoretische Studien, Schloss-Wolfsbrunnenweg 35, 69118 Heidelberg, Germany*
[5]*Zentrum für Astronomie der Universität Heidelberg, Astronomisches Recheninstitut, Mönchhofstr. 12-14, 69120 Heidelberg, Germany*
[6]*Max-Planck Institute for Astrophysics, Karl-Schwarzschild Str. 1, D-85748, Garching, Germany*

26 June 2012

ABSTRACT

We introduce the Phoenix Project, a set of ΛCDM simulations of the dark matter component of nine rich galaxy clusters. Each cluster is simulated at least at two different numerical resolutions. For eight of them, the highest resolution corresponds to ~ 130 million particles within the virial radius, while for one this number is over one billion. We study the structure and substructure of these systems and contrast them with six galaxy-sized dark matter haloes from the Aquarius Project, simulated at comparable resolution. This comparison highlights the approximate mass invariance of CDM halo structure and substructure. We find little difference in the spherically-averaged mass, pseudo-phase-space density, and velocity anisotropy profiles of Aquarius and Phoenix haloes. When scaled to the virial properties of the host halo, the abundance and radial distribution of subhaloes are also very similar, despite the fact that Aquarius and Phoenix haloes differ by roughly three decades in virial mass. The most notable difference is that cluster haloes have been assembled more recently and are thus significantly less relaxed than galaxy haloes, which leads to decreased regularity, increased halo-to-halo scatter and sizable deviations from the mean trends. This accentuates the effects of the strong asphericity of individual clusters on surface density profiles, which may vary by up to a factor of three at a given radius, depending on projection. The high apparent concentration reported for some strong-lensing clusters might very well reflect these effects. A more recent assembly also explains why substructure in some Phoenix haloes is slightly more abundant than in Aquarius, especially in the inner regions. Resolved subhaloes nevertheless contribute only $11 \pm 3\%$ of the virial mass in Phoenix clusters. Together, the Phoenix and Aquarius simulation series provide a detailed and comprehensive prediction of the cold dark matter distribution in galaxies and clusters when the effects of baryons can be neglected.

Key words: methods: N-body simulations – methods: numerical –dark matter – galaxies: haloes – galaxies:clustering

1 INTRODUCTION

The past two decades have witnessed the emergence of a paradigm for the origin of structure in the Universe. There is now strong evidence that the dominant forms of the matter-energy content are a combination of a mysterious form of "dark energy" that governs the late expansion of the Universe, and "dark matter" made up of some kind of non-baryonic, weakly interacting elementary particle left over from the Big Bang. Although the exact nature of the dark matter particle is unknown, astrophysical clues to its identity may be gained by studying its clustering properties on different scales. Considerable effort has been devoted to this task, and has led to the crafting of detailed theoretical predictions, especially for the case of particles with negligible thermal velocity, the cornerstone of the popular "cold dark matter" (CDM) theory. As a result, we now understand fairly well: (i) the statistics of CDM clustering on large scales and its dependence on the cosmological parameters (e.g., Jenkins et al. 1998; Springel et al. 2006); (ii) the dynamics of its incorporation into non-linear units ("haloes") (see, e.g., Wang et al. 2011, and references therein); and, at least empirically, (iii) its spatial distribution within such virialized structures (e.g., Frenk et al. 1985; Navarro et al. 1996, 1997, 2004, 2010).

Progress in this field has been guided by N-body simulations of ever increasing numerical resolution and dynamic range (e.g. Frenk et al. 1985; Navarro et al. 1997; Moore et al. 1999; Jing & Suto 2002; Navarro et al. 2004; Gao et al. 2004b;

⋆ Email:lgao@bao.ac.cn

Diemand et al. 2004a, 2007; Gao et al. 2008; Springel et al. 2008a; Stadel et al. 2009; Navarro et al. 2010). These simulations are essential to investigate highly non-linear scales such as the haloes of individual galaxies and galaxy groupings, where simple analytical approximations fail. A few key properties of CDM haloes are now widely agreed upon, at least when the effects of baryons are neglected: (a) the presence of a central density "cusp"; (b) strong deviations from spherical symmetry; (c) a remarkable similarity in the shape of the mass profiles; and (d) the presence of abundant substructure in the form of self-bound "subhaloes".

On the scale of individual galaxies, these key predictions have been confirmed and refined by the latest simulation work, in particular the Via Lactea simulation series (Diemand et al. 2007), the GHALO simulation (Stadel et al. 2009) and the Aquarius Project (Springel et al. 2008b,a; Navarro et al. 2010). For example, the central density cusp is now accepted to be shallower than hypothesized in some earlier work and mass profiles have been shown to be only approximately self-similar. Further, it is now clear that although subhaloes are subdominant in terms of total mass, they are still dense and abundant enough to dominate the dark matter annihilation radiation from a halo.

As shown by Springel et al. (2008a), the latter statement requires a detailed characterization of the substructure, including the internal properties of the subhaloes, their mass function, and their spatial distribution within the main halo. The Aquarius Project has provided compelling, if mainly empirical, guidance to each of these issues in the case of haloes similar to that of the Milky Way. For example, the subhalo mass function is well approximated by a power law, $dN/dM \propto M^{-1.9}$, with a normalisation, in scaled units, weakly dependent on halo mass (Gao et al. 2011a). In addition, subhaloes tend to avoid the central region of the main halo and are more prevalent in the outer regions. Interestingly, their spatial distribution appears independent of subhalo mass, a result that, if generally applicable, simplifies substantially the characterization of substructure. Finally, the internal structure of subhaloes obeys scaling laws similar to those of haloes in isolation but slightly modified by the effects of the tidal field of the main halo: subhaloes are "denser", reaching their peak circular velocity at radii roughly half that of their isolated counterparts.

Galaxy clusters are a promising venue for testing these predictions. The central cusp, for example, can be constrained by combining measurements of the stellar kinematics of the central galaxy with a lensing analysis of radial and tangential "arcs" near the cluster centre (e.g., Sand et al. 2002, 2004; Meneghetti et al. 2007; Newman et al. 2009; Zitrin et al. 2011). Outside the very centre, the cluster mass profile can be measured through weak lensing (see, e.g., Okabe et al. 2010; Oguri et al. 2011; Umetsu et al. 2011), X-ray studies of the hot intracluster medium (ICM; e.g, Buote et al. 2007), and, more recently, through the ICM Sunyaev-Ze'ldovich effect on the cosmic microwave background (see, e.g., Gralla et al. 2011). In many cases, including substructure seems *required* in order to obtain acceptable fits (e.g. Mao & Schneider 1998; Mao et al. 2004; Xu et al. 2009; Natarajan et al. 2007, 2009), implying that it should be possible to contrast observations directly with the CDM substructure predicted by simulations.

Such endeavour has so far been hindered by the lack of ultra-high-resolution dark matter simulations of galaxy clusters comparable to the Aquarius series. Indeed, the highest-resolution galaxy cluster simulations published to date have at most of order a few million particles within the virial radius (e.g. Jing & Suto 2000; Springel et al. 2001a; Diemand et al. 2004a; Reed et al. 2005), roughly one thousand times fewer than the best resolved Aquarius halo. None of these cluster simulations are thus able to address conclusively issues such as the structure of the central cusp or the properties of cluster substructure.

Although it may be tempting to appeal to the nearly self-similar nature of CDM haloes to extrapolate the Aquarius results to cluster scales, it is unclear what systematic uncertainties might be introduced through such extrapolation. Clusters are rare, dynamically young objects up to one thousand times more massive than individual galaxies. They thus trace scales where the CDM power spectrum differs qualitatively from that of galaxies. Precision work demands that the near self-similarity of dark haloes be scrutinized directly in order to provide definitive predictions for the CDM paradigm on cluster scales.

To this aim, we have carried out a suite of simulations designed to address these issues in detail. The Phoenix Project follows the design of the Aquarius Project and consists of zoomed-in resimulations of individual galaxy clusters drawn from a cosmologically representative volume. The simulations follow only the dark matter component of each cluster, and include the first simulation of a cluster-sized halo with more than one billion particles within the virial radius. Like the Aquarius Project on galaxy scales, the large dynamic range of these simulations allows us to probe not only the innermost regions of cluster haloes and thus the structure of the central cusp, but also the statistics, internal structure, and spatial distribution of cluster substructure over a mass range spanning seven decades.

Our paper is organized as follows. In Section 2, we describe our numerical techniques and introduce the simulation set. In Sec. 3 and Sec. 4 we discuss, respectively, the density profile and substructure properties of Phoenix haloes and compare them with those of Aquarius. Sec. 5 summarizes our main conclusions.

2 THE SIMULATIONS

The Phoenix Project consists of a series of simulations of 9 different galaxy clusters with masses exceeding $5 \times 10^{14}\, h^{-1}\, M_{\odot}$. These clusters were selected from a large cosmological volume and resimulated individually at varying resolution. Details of the resimulation procedure are given below.

2.1 Cosmology

All the simulations reported here adopt the cosmological parameters of the Millennium Simulation (Springel et al. 2005): $\Omega_{\rm M} = 0.25$, $\Omega_{\Lambda} = 0.75$, $\sigma_8 = 0.9$, $n_s = 1$, and a present-day value of the Hubble constant $H_0 = 100\, h\, {\rm km\ s^{-1}\ Mpc^{-1}} = 73\ {\rm km\ s^{-1}\ Mpc^{-1}}$. This is also the set of cosmological parameters adopted for the Aquarius project (Springel et al. 2008b), which targeted haloes a thousand times less massive. Although they are inconsistent with the latest CMB data (Komatsu et al. 2011) the differences are not large (the main difference is that a lower value of $\sigma_8 = 0.81$ is now preferred) and they are expected to affect only the abundance of cluster haloes rather than their detailed structure and substructure properties (Wang et al. 2012). This choice also has the advantage that any difference between Aquarius and Phoenix haloes can be traced to the different mass scales and not to variations in the cosmological model.

Name	$m_{\rm p}$ $[h^{-1}{\rm M}_\odot]$	M_{200} $[h^{-1}{\rm M}_\odot]$	r_{200} $[h^{-1}{\rm Mpc}]$	N_{200}	ϵ $[h^{-1}{\rm kpc}]$	$r_{\rm conv}$ $[h^{-1}{\rm kpc}]$
Ph-A-1	6.355×10^5	6.560×10^{14}	1.413	1,032,269,120	0.15	1.2
Ph-A-2	5.084×10^6	6.570×10^{14}	1.414	129,235,472	0.32	2.7
Ph-A-3	1.716×10^7	6.566×10^{14}	1.413	38,261,560	0.7	4.2
Ph-A-4	1.373×10^8	6.593×10^{14}	1.415	4,802,516	2.8	9.4
Ph-B-2	6.127×10^6	8.255×10^{14}	1.526	134,718,112	0.32	3.0
Ph-B-4	1.656×10^8	8.209×10^{14}	1.522	4,956,688	2.8	10.7
Ph-C-2	4.605×10^6	5.495×10^{14}	1.386	119,324,008	0.32	2.6
Ph-C-4	1.182×10^8	5.549×10^{14}	1.383	4,696,046	2.8	9.2
Ph-D-2	4.721×10^6	6.191×10^{14}	1.386	130,529,200	0.32	2.7
Ph-D-4	1.373×10^8	6.162×10^{14}	1.384	4,488,330	2.8	9.4
Ph-E-2	4.425×10^6	5.969×10^{14}	1.369	130,529,200	0.32	2.4
Ph-E-4	1.017×10^8	5.923×10^{14}	1.366	5,824,375	2.8	8.4
Ph-F-2	4.425×10^6	7.997×10^{14}	1.509	129,221,216	0.32	2.8
Ph-F-4	1.682×10^8	8.039×10^{14}	1.512	4,779,008	2.8	10.3
Ph-G-2	8.599×10^6	1.150×10^{15}	1.704	133,730,958	0.32	3.2
Ph-G-4	2.907×10^8	1.148×10^{15}	1.703	3,949,310	2.8	13.1
Ph-H-2	8.600×10^6	1.136×10^{15}	1.686	129,488,456	0.32	2.9
Ph-H-4	2.502×10^8	1.150×10^{15}	1.686	4,456,720	2.8	11.8
Ph-I-2	1.841×10^7	2.411×10^{15}	2.185	131,845,620	0.32	2.9
Ph-I-4	4.559×10^8	2.427×10^{15}	2.181	5,289,259	2.8	14.2

Table 1. Basic parameters of the Phoenix simulations. Each of the nine haloes is labelled as Ph-X-N, where the letter X (from A to I) identifies each halo, and N, which runs from 1 to 4, refers to the numerical resolution (1 is highest). The parameter $m_{\rm p}$ gives the particle mass in the high-resolution region that includes the cluster; M_{200} is the virial mass of the halo; r_{200} is the corresponding virial radius; and N_{200} states the number of particles inside r_{200}. The parameter ϵ is the Plummer-equivalent gravitational softening length, so that pairwise interactions are fully Newtonian when separated by a distance greater than 2.8ϵ. The last column lists the "convergence radius", $r_{\rm conv}$, outside which the circular velocity is expected to converge to better than 10%.

2.2 Cluster Sample and Resimulations

The Phoenix cluster sample is selected for resimulation from the Millennium Simulation friends-of-friends group catalog at $z=0$. Six clusters were selected at random from the 72 systems with virial[1] mass in the range $5 < M_{200}/10^{14}\,h^{-1}\,M_\odot < 10$. In order to sample the tail of rare rich clusters three further Phoenix clusters were selected from the nine Millennium halos which have $M_{200} > 10^{15}h^{-1}M_\odot$.

The initial conditions for resimulation were set up using a procedure analogous to that used for the Aquarius haloes and described in detail by Power et al. (2003) and Springel et al. (2008a). The only difference is that the initial displacements and velocities were computed using second-order Lagrangian perturbation theory, as described by Jenkins (2010). All nine haloes were resimulated at least twice using different numerical resolution (level 2 and level 4, respectively). At level 2 each cluster has between 120 and 135 million particles within the virial radius; at level 4 each system is made up of 4 to 6 million particles.

We have selected one of the clusters (Ph-A) for a numerical resolution study and have carried out an extra level-3 run (with roughly 40 million particles within r_{200}) and a flagship level-1 run, where we followed 4.05 billion high-resolution particles in total, 1.03 billion of which are found within r_{200} at $z=0$. For ease of reference we label the runs using the convention Ph-X-N, where X is a letter from A to I that identifies each individual cluster and N is a number from 1 to 4 that specifies the resolution level. The simulation parameters are summarized in Table 1. We have used for all runs the P-Gadget-3 code, a version of Gadget-2 (Springel et al. 2005) especially optimized for zoomed-in cosmological resimulations in distributed-memory massively-parallel computers. The code is identical to that used for the Aquarius Project (Springel et al. 2008b). The simulations were carried out on Deepcomp 7000 at the Supercomputer Center of the Chinese Academy of Science. The largest simulation, Ph-A-1, used 3 Tbs of memory on 1024 cores and took about 1.9 million CPU hours. The initial conditions were generated at the Institute for Computational Cosmology (Durham University).

The gravitational softening of each run was chosen following the "optimal" prescription of Power et al. (2003). It is kept fixed in comoving coordinates throughout each run and is listed in Table 1. Our highest-resolution run (Ph-A-1) has a nominal (Plummer-equivalent) spatial resolution of just $150\,h^{-1}$ pc.

Haloes are identified in each run using the friends-of-friends (FOF) group finding algorithm with linking length set to 20% of the mean interparticle separation (Davis et al. 1985). Substructure within FOF haloes is identified by SUBFIND (Springel et al. 2001b), a groupfinding algorithm that searches recursively for self-bound subhaloes. Both FOF and SUBFIND have been integrated within P-Gadget-3 and are run on-the-fly each time a simulation snapshot is created.

[1] We define the virial radius of a cluster, r_{200}, as that of a sphere of mean density 200 times the critical density for closure; $\rho_{\rm crit} = 3H_0^2/8\pi G$. The virial radius defines implicitly the virial mass of a cluster, M_{200}, and its virial velocity, $V_{200} = \sqrt{GM_{200}/r_{200}}$.

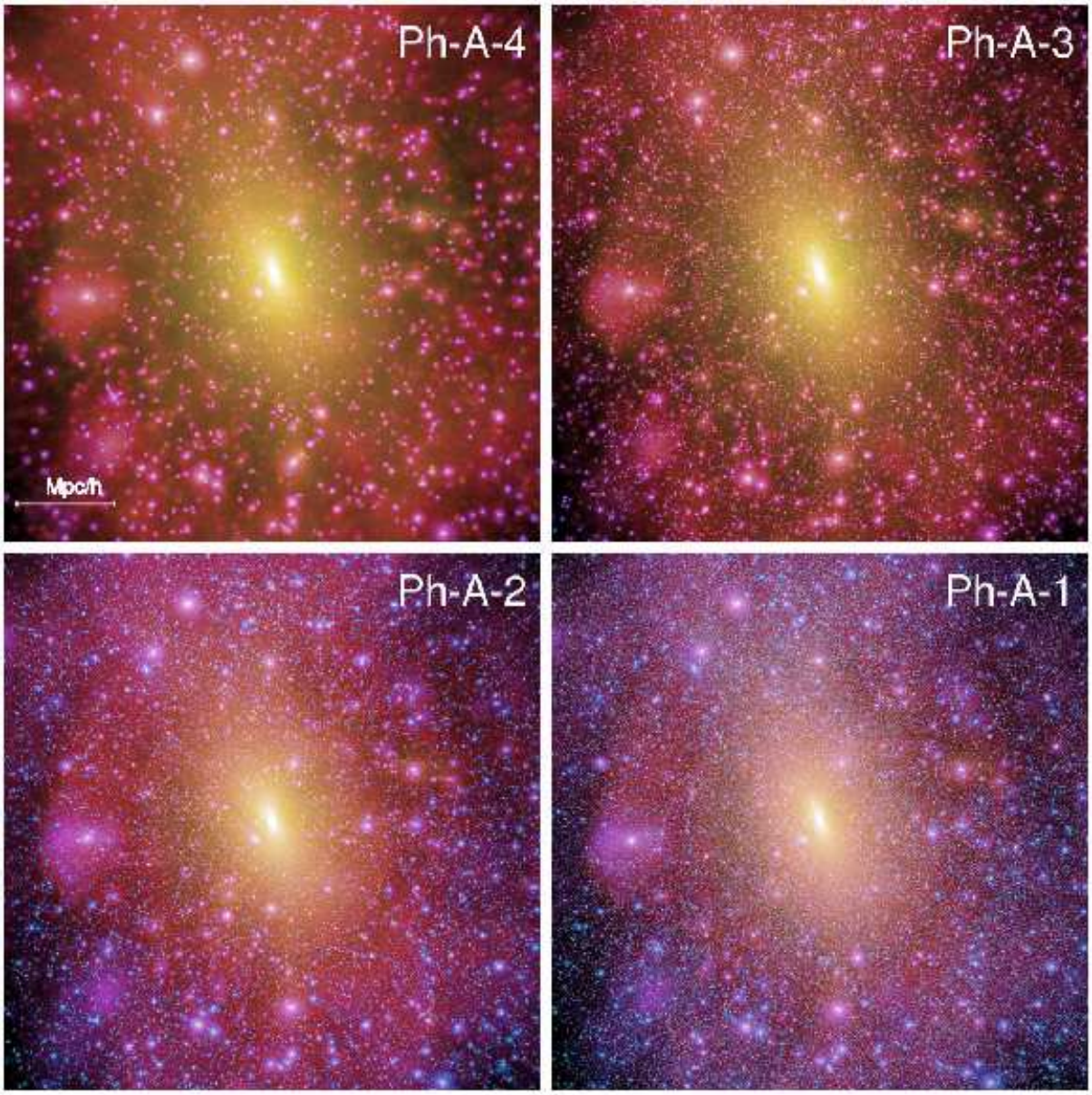

Figure 1. Images of cluster Ph-A at four different numerical resolutions. Each panel projects a cubic volume $5h^{-1}$ Mpc on a side. The brightness of each image pixel is proportional to the logarithm of the square of the dark matter density projected along the line of sight, and the hue encodes the local velocity dispersion density-weighted along the line of sight (see text for details). This rendering choice highlights the presence of substructure which, although abundant, contributes less than about 10% of the total mass within the virial radius.

We have stored for each run 72 snapshots uniformly spaced in $\log_{10} a$, starting at $a = 0.017$ ($a = 1/(1+z)$ is the expansion factor). The initial conditions are set at $z_{\rm init} = 63$ **for our level** 4 **and at** $z_{\rm init} = 79$ **for the rest**. The large number of outputs is designed to allow us in future work to implement semi-analytic models of galaxy formation in order to follow the evolution of the baryonic component of galaxies within rich clusters.

We list the basic structural parameters of Phoenix clusters at redshift $z = 0$ in Table 2. These include the peak circular velocity, $V_{\rm max}$, and the radius, $r_{\rm max}$, at which it is reached; the half-mass formation redshift, $z_{\rm h}$, when the main progenitor first reaches half the final halo mass; the concentration parameters, c and $c_{\rm E}$, obtained from the best-fit NFW (Navarro et al. 1996, 1997) and Einasto (1965) profiles, respectively; the figure of merit, $Q_{\rm NFW}$ and $Q_{\rm E}$, associated with each of those fits; and the Einasto "shape" parameter α. (See the Appendix for definitions corresponding to these fitting formulae and for details on the profile-fitting procedure.) $N_{\rm sub}$ is the total number of subhaloes with more than 20 particles identified by SUBFIND inside r_{200}; $f_{\rm sub}$ is the total mass contributed by these subhaloes, expressed as a fraction of the virial mass.

3 THE STRUCTURE OF PHOENIX CLUSTERS

We shall focus our analysis on the properties of Phoenix clusters at $z = 0$. Figure 1 shows Ph-A at the four different numerical resolutions. As in Springel et al. (2008a), this and other cluster images are constructed so that the brightness of each pixel is proportional

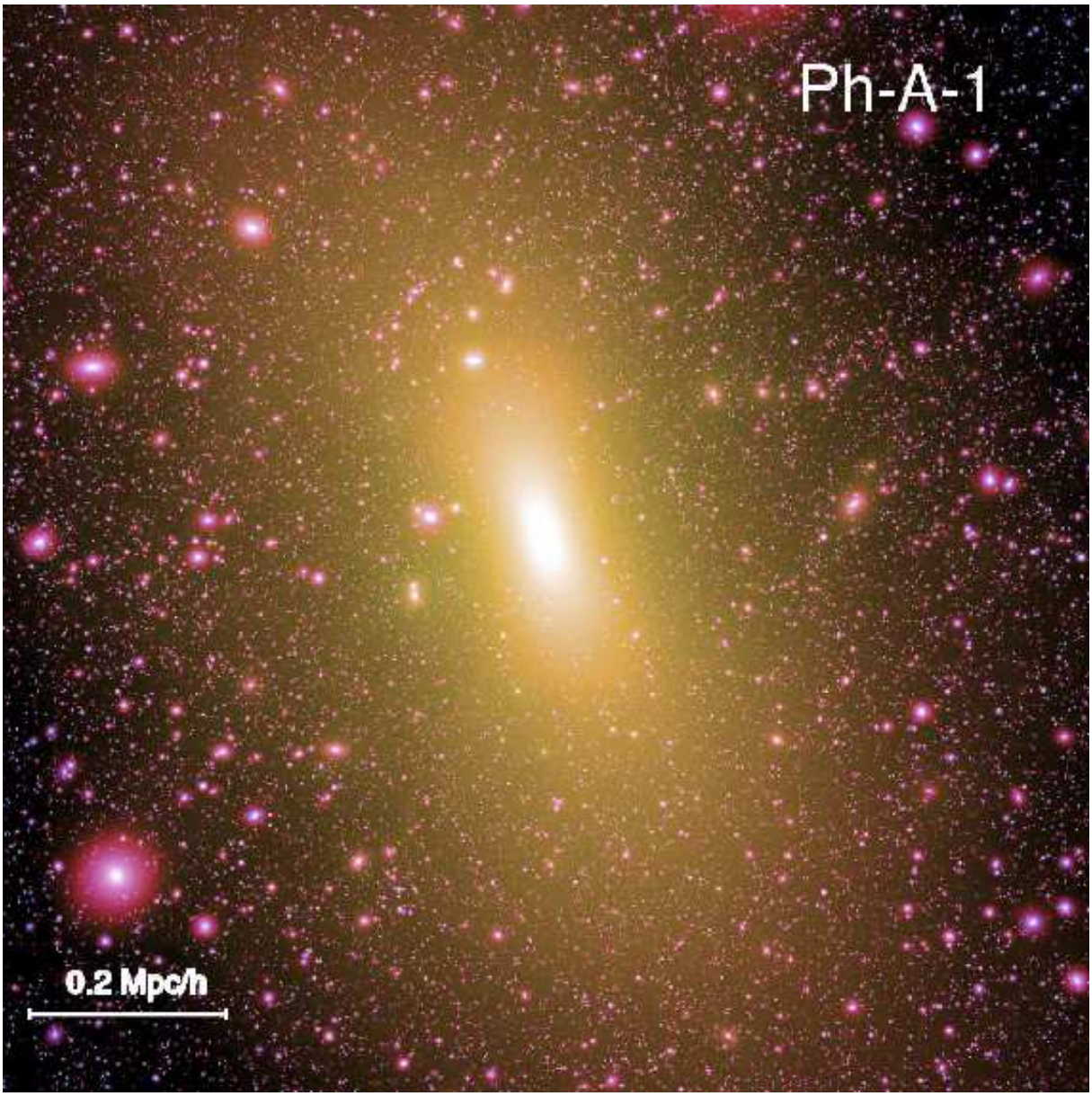

Figure 2. The inner $\sim 1h^{-1}$ Mpc of Ph-A-1. Color coding is as in Fig. 1. This figure illustrates clearly the strong asphericity of the halo; the presence of several nested levels of substructure, and the tendency of subhaloes to avoid the halo centre.

to the logarithm of the square of the dark matter density projected along the line of sight,

$$S(x,y) = \int \rho^2_{\rm loc}(\mathbf{r})\, dz \tag{1}$$

while the color hue encodes the mean dark matter velocity dispersion,

$$\sigma(x,y) = \frac{1}{S(x,y)} \int \sigma_{\rm loc}(\mathbf{r})\, \rho^2_{\rm loc}(\mathbf{r})\, dz \tag{2}$$

Here the local dark matter density, $\rho_{\rm loc}(r)$, and the local velocity dispersion, $\sigma_{\rm loc}(r)$, are estimated using an SPH kernel interpolation scheme.

Figure 1 shows that the main result of increasing the number of particles is the ability to resolve larger numbers of subhaloes. On the other hand, the main properties of the cluster, such as its shape and orientation, the overall mass profile, and even the location of the largest subclumps remain invariant in all four Ph-A realizations.

Fig. 2 is analogous to Fig. 1, but for the inner $\sim 1h^{-1}$ Mpc of Ph-A-1 (our highest resolution run). This image highlights the strong asphericity of the halo, as well as the presence of several nested levels of substructure (i.e., subhaloes within subhaloes). It also shows that subhaloes tend to avoid the central regions. These characteristics are shared with galaxy-sized haloes (Springel et al. 2008a), and appear to be typical of CDM haloes on all mass scales.

Fig. 3 is analogous to Fig. 1 but for all level-2 Phoenix haloes at $z = 0$. This figure shows that the main characteristics of Ph-A described above are common to all Phoenix clusters: strong asphericity; abundant substructure; and a marked difference between the spatial distribution of mass (which is highly concentrated) and that of subhaloes (which tend to avoid the central regions).

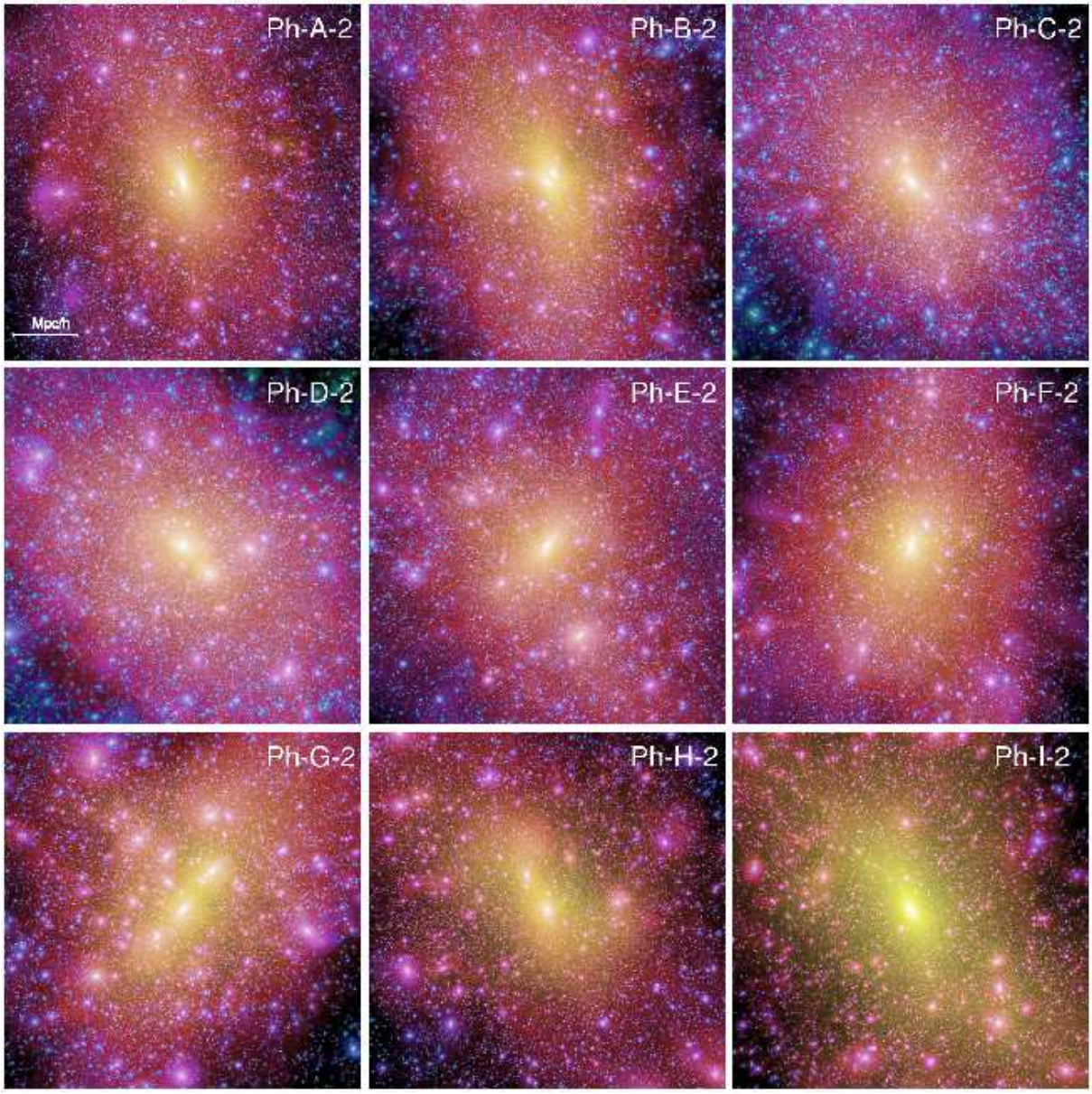

Figure 3. As Fig. 1, but for all level-2 Phoenix clusters at $z = 0$. Boxes are all $5h^{-1}$ Mpc on a side. Note that the appearance of several Phoenix clusters is suggestive of a transient evolutionary stage, characterized by the presence of a number of undissolved substructure groupings. Ph-G-2 is a particularly good example of this irregular structure which may be traced to its recent assembly time; this cluster has acquired half its mass since $z = 0.18$.

Fig. 3 also highlights an important characteristic of cluster-sized dark matter haloes: the presence of "multiple centres" traced by groups of subhaloes, as well as the overall impression that many systems are in a transient, unrelaxed stage of their evolution. This is expected, given the late assembly of the clusters: Ph-G-2, for example, assembled half its final mass after $z = 0.18$; the median half-mass assembly redshift for all Phoenix clusters is just $z = 0.56$. Ph-A, on the other hand, appears relaxed; this cluster has the highest formation redshift of our sample, $z_h \sim 1.2$.

The late assembly and concomitant departures from equilibrium are characteristics that set clusters apart from galaxy-sized haloes; for comparison, the median half-mass formation redshift of Aquarius haloes is $z \sim 2$. Table 2 lists two quantitative measures of departures from equilibrium: the fraction of mass in substructures, $f_{\rm sub}$, and the offset, $d_{\rm off}$, between the centre of mass of the halo and the location of the potential minimum expressed in units of the virial radius (for further discussion of these parameters see Neto et al. 2007). These correlate well with the formation redshift, z_h, and are significantly larger, on average, than in the galaxy-sized Aquarius haloes (see Table 3).

3.1 Mass Profiles

We explore in this section the spherically-averaged mass profiles of Phoenix haloes. We begin by using the four Ph-A realizations to assess the limitations introduced by finite numerical resolution. Fig. 4 shows the density profile, $\rho(r)$, as well as the radial dependence of the logarithmic slope, $\gamma = -d\ln\rho/d\ln r$, for Ph-A-1 through Ph-A-4. As discussed by Power et al. (2003) and Navarro et al. (2010), the mass profiles of simulated haloes are robustly determined in

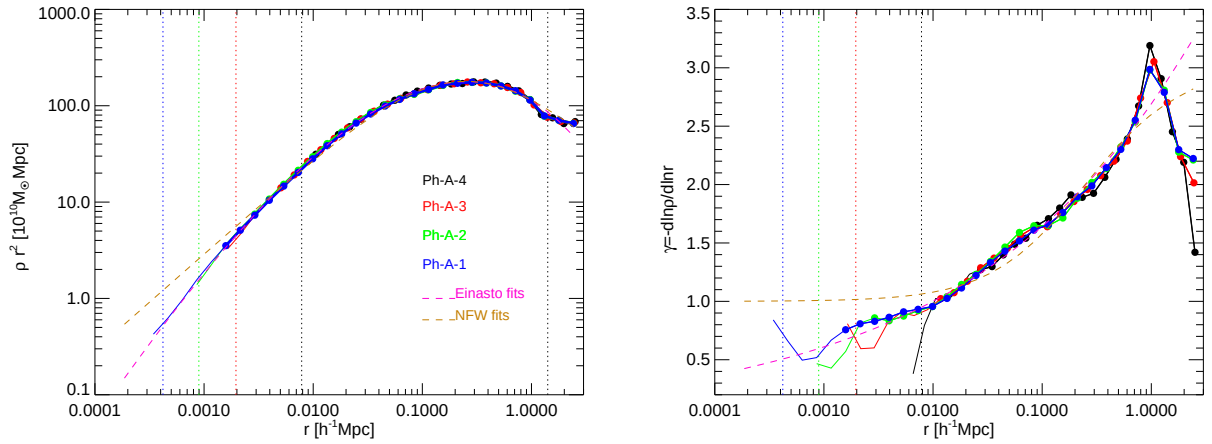

Figure 4. *Left panel*: Spherically-averaged density profile of halo Ph-A at $z = 0$. Different colors correspond to the four different resolution runs listed in Table 1. The panel on the left shows the density multiplied by r^2 in order to enhance the dynamic range of the plot. Each profile is shown with a thick line connecting filled circles from the "convergence radius", $r_{\rm conv}$, outwards (Power et al. 2003). Thin curves extend the profiles inwards down to $r = 2\epsilon$, where ϵ is the Plummer-equivalent gravitational softening length. Vertical dotted lines indicate, for each run, 2.8ϵ, the distance beyond which pairwise particle interactions are fully Newtonian. Note the excellent numerical convergence achieved for each simulation outside their $r_{\rm conv}$. An NFW profile with concentration $c = 5.63$ (thin dashed brown line) and an Einasto profile with $\alpha = 0.22$ and $c_{\rm E} = 5.59$ (thin dashed magenta line) are also shown for comparison. *Right panel*: Logarithmic slope ($\gamma = -d\ln\rho/d\ln r$) of the density profile as a function of radius. Colors and line types are the same as in the left panel. Note again the excellent convergence achieved in all runs at radii outside the convergence radius, $r_{\rm conv}$.

Name	$V_{\rm max}$ [km s^{-1}]	$r_{\rm max}$ [h^{-1}Mpc]	$z_{\rm h}$	$c_{\rm E}$	c	$Q_{\rm E}$	$Q_{\rm NFW}$	α	$N_{\rm sub}$	$f_{\rm sub}$	$d_{\rm off}$
Ph-A-1	1521.82	0.55	1.17	5.59	5.63	0.037	0.093	0.215	192,206	0.080	0.04
Ph-A-2	1527.24	0.55	1.17	5.72	5.96	0.039	0.075	0.216	26,896	0.071	0.04
Ph-A-3	1529.41	0.56	1.17	5.69	6.04	0.038	0.061	0.218	8,478	0.062	0.04
Ph-A-4	1538.88	0.59	1.17	5.71	6.14	0.052	0.063	0.219	1,049	0.049	0.04
Ph-B-2	1624.52	0.53	0.46	4.41	4.19	0.127	0.108	0.235	38,659	0.108	0.02
Ph-B-4	1623.12	0.56	0.46	4.40	4.06	0.107	0.117	0.276	1,657	0.081	0.02
Ph-C-2	1294.19	0.65	0.76	4.27	5.11	0.077	0.104	0.181	33,529	0.114	0.06
Ph-C-4	1310.19	0.78	0.76	4.34	4.72	0.085	0.112	0.185	1,489	0.095	0.06
Ph-D-2	1393.13	0.68	0.46	3.88	4.08	0.122	0.086	0.205	38,199	0.124	0.05
Ph-D-4	1436.10	0.65	0.46	4.03	4.34	0.136	0.127	0.212	1,491	0.093	0.05
Ph-E-2	1385.78	0.65	0.91	3.48	5.19	0.067	0.135	0.149	33,678	0.101	0.04
Ph-E-4	1399.96	0.68	0.91	4.02	4.82	0.048	0.079	0.181	1,547	0.070	0.04
Ph-F-2	1543.27	0.60	1.1	3.81	4.61	0.053	0.048	0.186	31,247	0.095	0.05
Ph-F-4	1559.44	0.62	1.1	4.00	4.54	0.059	0.057	0.203	1,547	.075	0.05
Ph-G-2	1561.75	1.06	0.18	0.78	3.33	0.100	0.221	0.097	42,528	0.168	0.17
Ph-G-4	1599.17	1.04	0.18	1.10	2.98	0.109	0.164	0.116	1,586	0.140	0.17
Ph-H-2	1676.43	1.14	0.21	1.98	4.66	0.155	0.212	0.117	35,048	0.095	0.1
Ph-H-4	1710.19	1.14	0.21	2.75	3.59	0.109	0.115	0.178	1,437	0.069	0.1
Ph-I-2	2236.05	1.03	0.56	4.18	4.86	0.041	0.059	0.190	35,754	0.102	0.02
Ph-I-4	2269.09	1.05	0.56	4.48	5.02	0.045	0.051	0.208	1,641	0.073	0.02

Table 2. Basic structural parameters of Phoenix clusters at $z = 0$. The leftmost column labels each run, as in Table 1; the second and third columns list the peak circular velocity, $V_{\rm max}$, and the radius, $r_{\rm max}$, at which it is reached. The concentration parameters of the best NFW (Navarro et al. 1996, 1997) and Einasto (Einasto 1965) fits are listed under c and $c_{\rm E}$, respectively. $Q_{\rm NFW}$ and $Q_{\rm E}$ are the figures of merit of the best NFW and Einasto fits, respectively. The column labelled α lists the Einasto shape parameter. $N_{\rm sub}$ denotes the total number of subhaloes with more than 20 particles identified within r_{200}; $f_{\rm sub}$ is the fraction of the virial mass contributed by such subhaloes; and $d_{\rm off}$ is the distance from the gravitational potential minimum to the centre of mass of particles within the virial radius, in units of r_{200}.

Name	$\langle z_h \rangle$	$\langle d_{\rm off} \rangle$	$\langle f_{\rm sub} \rangle$	$\langle \alpha \rangle$	$\langle Q_{\rm min} \rangle$	$\langle C_\chi \rangle$	$\langle \chi \rangle$	$\langle N_m \rangle$	$\langle s \rangle$	$\langle N_v \rangle$	$\langle d \rangle$
Phoenix	0.65 $\pm$0.36	0.061 $\pm$0.047	0.109 $\pm$0.027	0.175 $\pm$0.046	0.086 $\pm$0.041	1.75 $\pm$0.29	$-$1.86 $\pm$0.04	7866 $\pm$965	$-$0.97 $\pm$0.02	3984 $\pm$317	$-$3.32 $\pm$0.10
Aquarius	1.65 $\pm$0.65	0.032 $\pm$0.011	0.071 $\pm$0.022	0.159 $\pm$0.022	0.048 $\pm$0.012	2.19 $\pm$0.14	$-$1.82 $\pm$0.02	5092 $\pm$677	$-$0.94 $\pm$0.02	4033 $\pm$500	$-$3.13 $\pm$0.09

Table 3. Comparison of the average properties of the six galaxy-sized Aquarius haloes and the nine cluster-sized Phoenix haloes. Sample averages are listed for each quantity together with the rms dispersion around the mean. The first column identifies the simulation set; z_h is the half-mass formation redshift; $d_{\rm off}$ and $f_{\rm sub}$ are the dynamical relaxation diagnostics introduced in Table 2; α is the best-fit Einasto shape parameter and $Q_{\rm min}$ the goodness of fit measure (Sec. 6); C_χ and χ are the parameters of power-law fits to the pseudo-phase-space density profile (eq. 3); N_m and s describe the power-law fits to the subhalo mass function, $N(>\mu) = N_m\,(\mu/10^{-6})^s$ (eq. 4); N_v and d those corresponding to fits of the form, $N(>\nu) = N_v\,(\nu/0.025)^d$, to the subhalo velocity function (eq. 5).

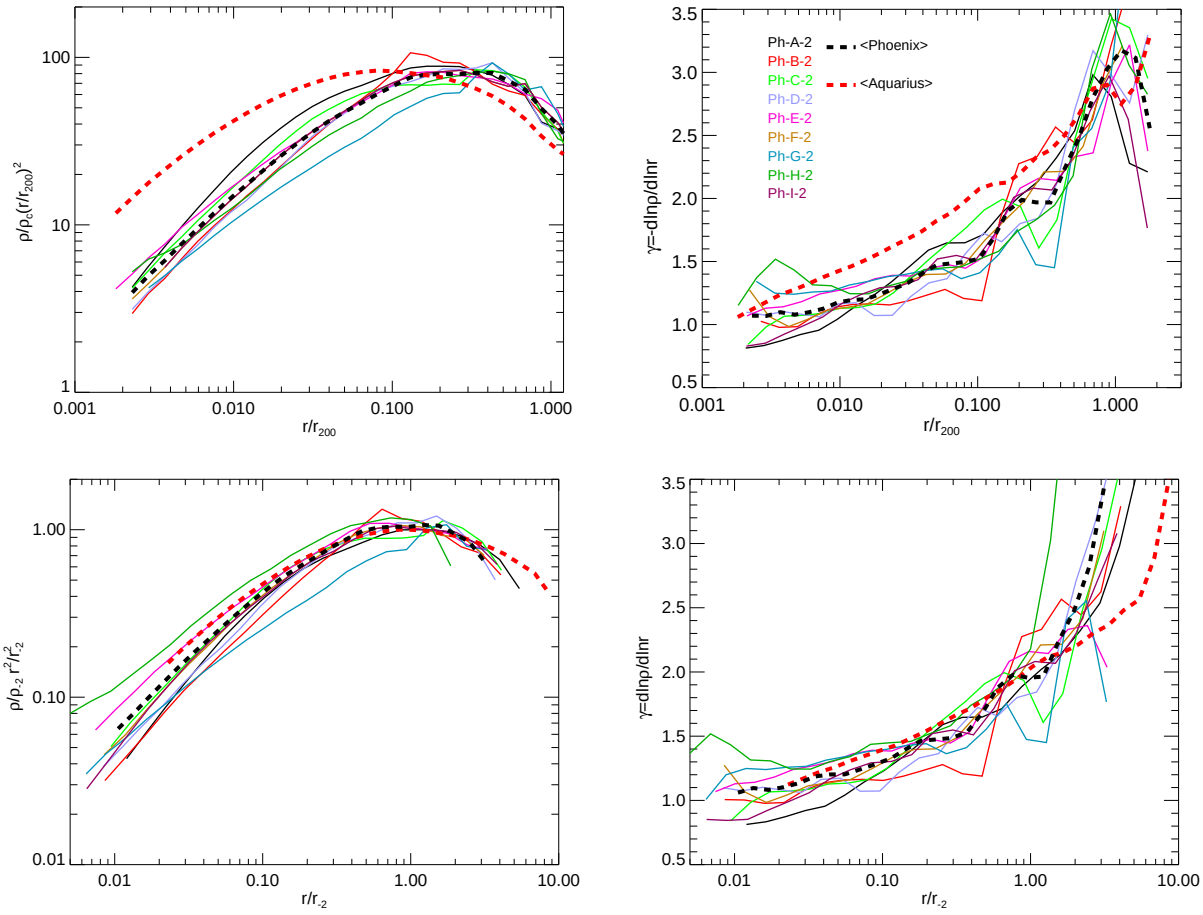

Figure 5. Spherically-averaged density (left panels) and logarithmic slope (right panels) of all level-2 Phoenix haloes as a function of radius. Radii have been scaled to the virial radius of each halo in the top panels and to the "scale radius", r_{-2}, of the best-fit Einasto profile in the bottom panels. Profiles are plotted down to the convergence radius, $r_{\rm conv}$. The thick dashed black line shows the average density profile of all Phoenix haloes, computed after stacking the nine haloes, each scaled to its own virial mass and radius. The thick red dashed line shows the result of the same stacking procedure, but applied to the Aquarius haloes.

regions where the two body-relaxation time exceeds the age of the Universe. This constraint defines a "convergence radius", $r_{\rm conv}$, outside which the circular velocity, $V_c = (GM(<r)/r)^{1/2}$, is expected to converge to better than 10%. Since V_c is a cumulative measure we expect $r_{\rm conv}$ to be a *conservative* indicator of the innermost radius where local estimates of the density, $\rho(r)$, converge to better than 10%.

This is indeed the case for Ph-A, as shown in Fig. 4. The left panel shows $\rho(r)$, multiplied by r^2 in order to remove the dominant radial trend so as to enhance the dynamic range of the plot. Thick lines highlight the radial range of the profile outside the convergence radius; the density clearly converges to better than 10% at radii greater than $r_{\rm conv}$. In those regions the logarithmic slope γ is also robustly and accurately determined. We conclude that $r > r_{\rm conv}$ is a simple and useful prescription that identifies the regions unaffected by numerical limitations. We list $r_{\rm conv}$ for all Phoenix runs in Table 1.

The thin dashed lines in Fig.4 indicate the best-fit NFW

(brown) and Einasto (magenta) profiles, computed as described in the Appendix. The NFW shape is fixed in this log-log plot, whereas the Einasto shape is controlled by the parameter α, which is found to be 0.215 by the fitting procedure when applied to the Ph-A-1 profile. This figure suggests that the shape of the mass profile deviates slightly but systematically from the NFW profile. Although it is possible to obtain excellent fits over the resolved radial range with the NFW formula (typical residuals are less than $\sim 10\%$), there is a clear indication that the density profile near the centre is shallower than the asymptotic r^{-1} NFW cusp. In agreement with results from the Aquarius Project (Navarro et al. 2010), there is little indication that the central density cusp of Ph-A is approaching a power-law; the profile becomes gradually shallower all the way in to the innermost resolved radius. This radial trend is very well described by the Einasto profile.

Fig. 5 shows the density profiles of all level-2 Phoenix haloes, in a format similar to that of Fig. 4. The top panels show profiles with radii scaled to the virial radius of each cluster, whereas those at the bottom show radii in units of the "scale radius", r_{-2}, of the best Einasto fit. Profiles are shown from the convergence radius, $r_{\rm conv}$, outwards.

In general, the density profiles of Phoenix clusters become gradually shallower towards the centre; from $\gamma \sim 3$ in the outer regions to an average value of $\gamma \sim 1$ at the innermost resolved radius. This behaviour is similar to that of Aquarius haloes, whose average profile is shown by the thick red dashed lines in Fig. 5. The large difference between Aquarius and Phoenix seen in the top panels of this figure just reflect the different concentration[2] of cluster- and galaxy-sized haloes. Indeed, when radii are scaled to r_{-2}, *the average Phoenix and Aquarius profiles are basically indistinguishable from each other*.

This is confirmed quantitatively by the best-fit Einasto parameters of these average profiles (listed in Table 3). The average Phoenix halo is only slightly worse fit by an Einasto profile than Aquarius, as shown by the $Q_{\rm min}$ goodness-of-fit measure (6.5% vs 1.8%, respectively). There is also a slight difference in shape parameter; the average Phoenix cluster has $\alpha = 0.175$ whereas the average Aquarius halo has $\alpha = 0.159$, in agreement with previously reported trends (Gao et al. 2008).

One aspect in which Phoenix and Aquarius haloes do differ is the halo-to-halo scatter: the dispersion in the Einasto parameter α is twice as large for clusters as for galaxy-sized haloes (Table 3). This may be readily seen in Fig. 5: Ph-A-2, for example, follows the steady decline in γ towards the centre exhibited by Ph-A-1 (and characteristic also of Aquarius haloes), whereas in other cases, such as Ph-H-2, γ stays roughly constant over a wide radial range near the centre.

The latter behaviour is poorly captured by the Einasto or NFW fitting formulae, and leads to larger residuals and figure-of-merit values for the best fits. NFW and Einasto best-fit residuals are shown in Fig. 6; per bin deviations of up to 40% from NFW and $\sim 20\%$ from Einasto fits are not uncommon for Phoenix clusters.

These deviations may be traced to transient departures from equilibrium induced by the recent formation of many Phoenix clusters. For example, one of the worst offenders is Ph-H-2, which accreted half its final mass since $z = 0.21$ and whose unrelaxed appearance is obvious in Fig. 3. In contrast, Ph-A-2, the cluster with highest formation redshift of the Phoenix series ($z_{\rm h} = 1.17$) is very well fit by both the Einasto and NFW profiles, with average residuals of only $\sim 3\%$ and $\sim 6\%$, respectively. Indeed, a well defined correlation may be seen in Table 2 between quantitative measures of departures from equilibrium, such as the centre offset, $d_{\rm off}$, or the mass fraction in the form of substructure, $f_{\rm sub}$, and the average residuals from the best NFW and Einasto fits. On average, both indicators are substantially smaller for Aquarius than for Phoenix (Table 3), as expected. The higher formation redshift of galaxy-sized haloes means that they are closer to dynamical equilibrium than recently-assembled cluster haloes.

3.2 Pseudo-Phase-Space Density and Velocity Anisotropy

The similarity in the mass profiles of galaxy- and cluster-sized CDM haloes highlighted in the previous subsection extends to their dynamical properties. We show this by comparing the spherically averaged pseudo-phase-space density (PPSD) profiles of Phoenix and Aquarius haloes. The PPSD, ρ/σ^3, is dimensionally identical to the phase-space density, but not strictly a measure of it. (Here the velocity dispersion, $\sigma(r)$, is defined as the square root of twice the specific kinetic energy in each spherical shell.) It is well known that PPSD profiles are well approximated by a simple power-law, $\rho/\sigma^3 \propto r^\chi$ (Taylor & Navarro 2001), intriguingly similar to the secondary-infall self-similar solutions of Bertschinger (1985), where the exponent, $\chi = -1.875$ (see also Ludlow et al. 2010, and references therein).

PPSD profiles for all level-2 Phoenix clusters are shown in Fig. 7, and compared with the average PPSD for Aquarius haloes. Since clusters are denser and have higher velocity dispersions than galaxy-sized haloes, we scale all profiles to the scale radius, r_{-2}, of each halo. Together with the density at this characteristic radius, ρ_{-2}, these quantities define a characteristic velocity, $V_{-2} = (G\rho_{-2})^{1/2} r_{-2}$, that allows us to compare PPSD profiles of haloes of widely different mass in a meaningful way.

The top panel of Fig. 7 shows that, in these scaled units, Aquarius and Phoenix have very similar PPSD profiles. The similarity extends over the range $0.06 < r/r_{-2} < 4$ where both simulation sets give converged results. (Note that Phoenix profiles actually probe radii interior to $0.06\,r_{-2}$ because of their lower concentration.) Table 3 lists the average parameters (and their dispersion) of power-law fits of the form

$$\frac{\rho}{\sigma^3} = C_\chi \frac{\rho_{-2}}{V_{-2}^3} \left(\frac{r}{r_{-2}}\right)^\chi, \qquad (3)$$

where $C_\chi = (\sigma(r_{-2})/V_{-2})^3$. Fits are carried out over the length range $0.06 < r/r_{-2} < 4$ for each halo. On average, both the slope and the normalisation of Aquarius and Phoenix PPSD profiles are almost indistinguishable emphasizing again the structural similarity between cluster- and galaxy-sized haloes.

At the same time, the scatter is larger in the Phoenix sample than in Aquarius (Table 3), highlighting again the larger halo-to-halo variation of cluster profiles. This may also be appreciated in the bottom panel of Fig. 7, where residuals from the self-similar $r^{-1.875}$ power law are shown. Although PPSD profiles scatter above and below the self-similar solution depending on the individual dynamical state of each cluster, the PPSD profile of cluster haloes seem to be, on average, indistinguishable from that of galaxy-sized haloes.

We reach a similar conclusion when comparing the velocity anisotropy profiles of Phoenix clusters with those of Aquarius

[2] The concentration is defined as r_{200}/r_{-2}, where r_{-2} is the radius at which the logarithmic slope γ has the isothermal value of 2. This indicates the location of the maximum of the curves shown in Fig. 5.

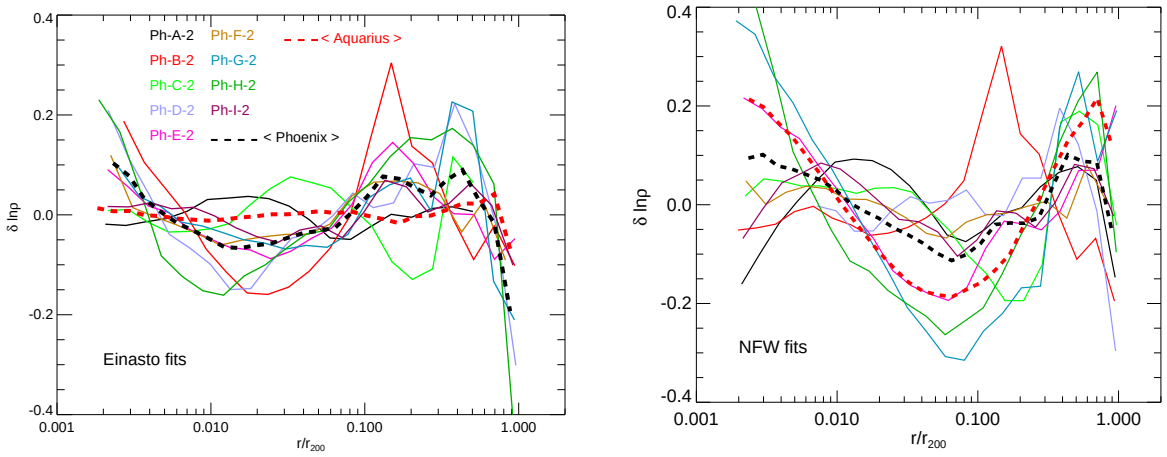

Figure 6. Residuals from the best Einasto (left panel) and NFW (right panel) profile fits for all level-2 Phoenix haloes. Colors and line types are as in Fig.5. The thick black dashed curve corresponds to the composite profile obtained after stacking all 9 Phoenix level-2 runs. The red thick dashed curve corresponds to the same composite profile, but for the 6 galaxy-sized level-2 Aquarius haloes.

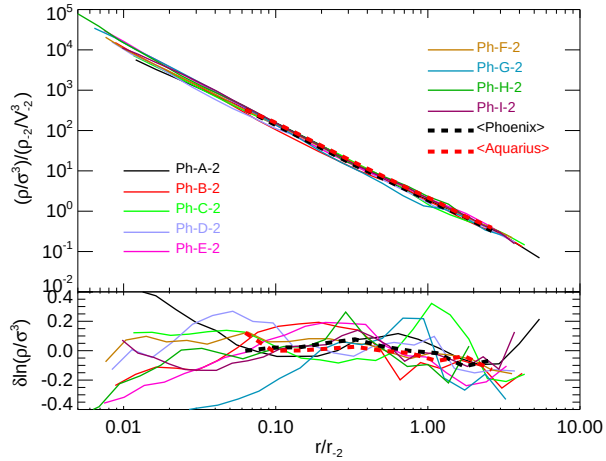

Figure 7. Spherically averaged pseudo-phase-space density (PPSD; ρ/σ^3) of all level-2 Phoenix haloes as a function of radius. Profiles are plotted down to the convergence radius, $r_{\rm conv}$. Radii are given in units of the scale radius, r_{-2}, of the best-fit Einasto profile for each halo. Densities are scaled to $\rho_{-2} = \rho(r_{-2})$, and velocity dispersions, $\sigma(r)$, to the characteristic velocity $V_{-2} = (G\rho_{-2})^{1/2} r_{-2}$. The thick dashed lines shows the average PPSD of all Phoenix (black) and Aquarius (red) haloes plotted over the converged radial range common to both simulation series: $0.06 \leq (r/r_{-2}) \leq 4$, respectively. The bottom panel shows residuals from a simple $r^{-1.875}$ power-law fit.

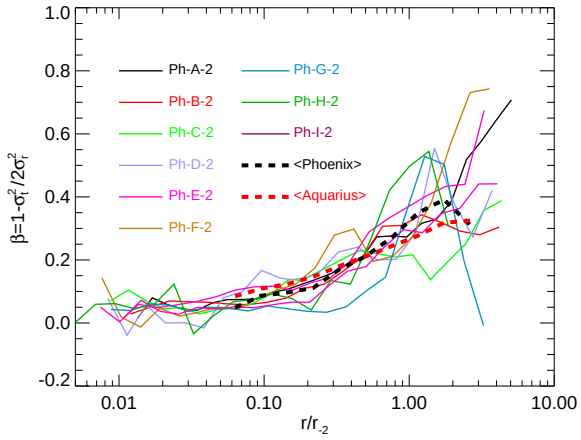

Figure 8. Velocity anisotropy profiles of all level-2 Phoenix haloes. Radii are expressed in units of the scale radius, r_{-2}, of the best-fit Einasto profile. Profiles are plotted down to the convergence radius, $r_{\rm conv}$. The thick dashed lines show the average anisotropy profile of all Phoenix (black) and Aquarius (red) haloes over the radial range where both give converged results $(0.06 \leq (r/r_{-2}) \leq 4)$.

haloes (Fig. 8). Aside from a slightly larger scatter, the velocity anisotropy, which measures the ratio of the kinetic energy in tangential and radial motions, increases gently from the centre, where haloes are nearly isotropic, to the outer regions, where radial motions dominate. Phoenix and Aquarius haloes again seem indistinguishable from each other regarding velocity anisotropy when compared over their converged radial range.

3.3 Projected Profiles

The preceding discussion highlights the mass invariance of the structure of CDM haloes, but it also makes clear that the dynamical youth of clusters limits the validity of simple fitting formulae to describe their instantaneous mass profiles. This complication must be taken into account when comparing observational estimates of individual cluster mass profiles with the profiles expected in a CDM-dominated Universe. Stacking clusters in order to obtain an "average" cluster profile might offer a way of circumventing this difficulty. This should smooth out local inhomogeneities in the mass distribution and average over different dynamical states to produce a more robust measure of the shape of the mass profile.

Aside from dynamical youth, another issue that complicates the interpretation of observations is the fact that, due to the cluster's asphericity, *projected* mass profiles, such as those measured through gravitational lensing, may differ substantially from simple projections of the 3D spherically-averaged profiles discussed above.

Depending on the line of sight a cluster may appear more or

less massive within a given radius, leading to biases in the cluster's estimated mass, concentration, and even the shape of its density profile. We illustrate this in Fig. 9, where we plot the surface density profile of two Phoenix clusters, Ph-A-2 and Ph-I-2, each projected along 20 different random lines of sight. The aspherical nature of the clusters results in large variations (up to a factor of 3) in the surface density in the inner regions. For comparison, we also show in Fig. 9 the result of a weak and strong-lensing analysis of a stack of four massive clusters by Umetsu et al. (2011). The mass of the stacked cluster lies between that of Ph-A and Ph-I, which explains why, on average, Ph-A $\Sigma(R)$ profiles lie below the observed data whereas the opposite applies to Ph-I.

In agreement with earlier work (see, e.g., Corless & King 2007; Sereno et al. 2010; Oguri et al. 2010, and references therein), Fig. 9 suggests that substantial biases may be introduced by projection effects on estimates of cluster parameters, especially when reliable data are restricted to the inner regions of a cluster. For example, fitting the inner $500\,h^{-1}$ kpc of the Ph-A-2 projected profile with an NFW profile results in mass and concentration (M_{200}, c) estimates that vary from ($5.4\times10^{14}\,h^{-1}\,M_\odot$, 4.8) to ($7.3\times10^{14}\,h^{-1}\,M_\odot$, 9.8) when using the projections that maximize or minimize the inner surface density, respectively (see Fig. 9). The corresponding numbers for Ph-I-2 are ($1.8\times10^{15}\,h^{-1}\,M_\odot$, 4.1) and ($3.0\times10^{15}\,h^{-1}\,M_\odot$, 7.1). Comparing these numbers with those listed in Tables 1 and 2 we see that variations as large as $\sim30\%$ in the mass and $\sim60\%$ in the concentration may be introduced just by projection effects[3].

We explore this further in Fig. 10, where the small dots show the mass-concentration estimates for 500 random projections of each level-2 Phoenix cluster. Large symbols correspond to the 3D estimates listed in Tables 1 and 2. The black diamond symbol indicates the M_{200}-c estimate for the stack of 4 strong-lensing clusters presented by Umetsu et al. (2011). This figure again emphasizes the importance of projection effects; for example, 12% of random projections result in concentration overestimates larger than 25%. Although an exhaustive analysis of such biases is beyond the scope of the present paper, the results in Figs. 9 and 10 suggest that there is no substantial difficulty matching the surface density profile of lensing clusters such as those studied by Umetsu et al. (2011). Our interpretation thus agrees with that reached by a number of recent studies (see, e.g., Oguri et al. 2011; Okabe et al. 2010; Gralla et al. 2011; Umetsu et al. 2011), which conclude that there is no obvious conflict between the concentration of lensing-selected clusters and those of ΛCDM haloes once projection effects are taken into account. Interestingly, despite the large variations in surface density alluded to above, the *shape* of the surface density profile is quite insensitive to projection effects. We show this in the right-hand panels of Fig. 9; the weak dependence of $\gamma_p(R)$ on projection may thus be profitably used to assess the consistency of theoretical predictions with cluster mass profiles. For illustration, we compare in the same panels the logarithmic slope of the projected profile, $\gamma_p = d\ln\Sigma(R)/d\ln R$, with the stacked cluster data of Umetsu et al. (2011). Despite the fact that the mass of the simulated and observed clusters are different and that no scaling has been applied, there is clearly quite good agreement between observation and Phoenix clusters, supporting our earlier conclusion. Available data on individual clusters are bound to improve dramatically with the advent

[3] Note that variations may actually be larger, because these estimates neglect the possible contribution of the large-scale mass distribution along the line-of-sight.

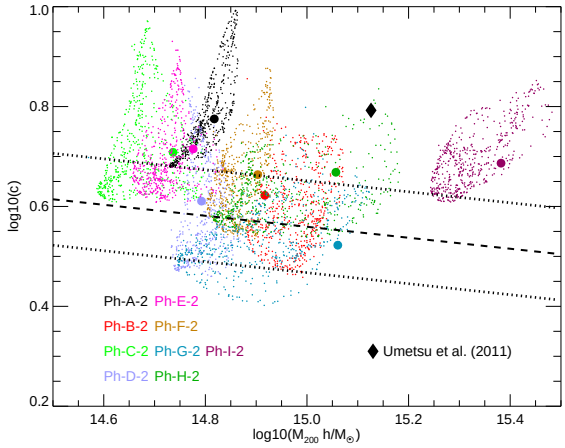

Figure 10. Cluster virial mass vs concentration estimated from fits to the projected density profiles of level-2 Phoenix haloes in the radial range $R < 500\,h^{-1}$ kpc. A total of 500 random projections are used for each halo. The large filled circles indicate the true value of the virial mass and concentration of the cluster, obtained from NFW fits to the 3D spherically-averaged profile (see Appendix and Table 2). The dashed curve flanked by dotted lines shows the fit to the mass-concentration relation derived by Neto et al. (2007). Note that projection effects lead to significant bias in the mass and concentration. , which are underestimated on average by $8.5\pm17\%$ and $0.4\pm20\%$, respectively, where the "error" is the rms of all projections for the 9 clusters. The black diamond symbol indicates the M_{200}-c estimate for a stack of 4 strong-lensing clusters taken from Umetsu et al. (2011).

of surveys such as CLASH with the Advanced Camera for Surveys onboard the Hubble Space Telescope (Postman et al. 2011). These surveys will enable better constraints on the shape of the inner mass profile of individual rich clusters and it is therefore important to constrain how projection effects may affect them. Fig. 11 shows the distribution of γ_p at two projected radii, $R = 3$ and $10\,h^{-1}$ kpc. The histograms are computed after choosing 500 random lines of sight for each of our 9 level-2 Phoenix haloes. On average, cluster projected profiles flatten steadily towards the centre, from $\langle\gamma_p\rangle = 0.35$ to 0.25 in that radial range, but with fairly large dispersion; the rms is $\sigma_{\gamma_p} = 0.054$ and 0.091 at $R = 10$ and $3\,h^{-1}$ kpc respectively. Because of the large dispersion it is unlikely that observations of a single cluster can lead to conclusive statements about the viability of CDM; however, it should be possible to use this constraint fruitfully once data for a statistically significant number of clusters become available.

4 THE SUBSTRUCTURE OF PHOENIX CLUSTERS

As may be seen from the images presented in Fig. 3, substructure is ubiquitous in Phoenix clusters. We have used SUBFIND (Springel et al. 2001b) to identify and characterize self-bound structures (subhaloes) within the virial radius of the main halo. We discuss below the mass function, spatial distribution, and internal properties of subhaloes in Phoenix. Since our main goal is to explore the mass invariance of the properties of CDM haloes, we contrast these results with those obtained for the galaxy-sized Aquarius haloes.

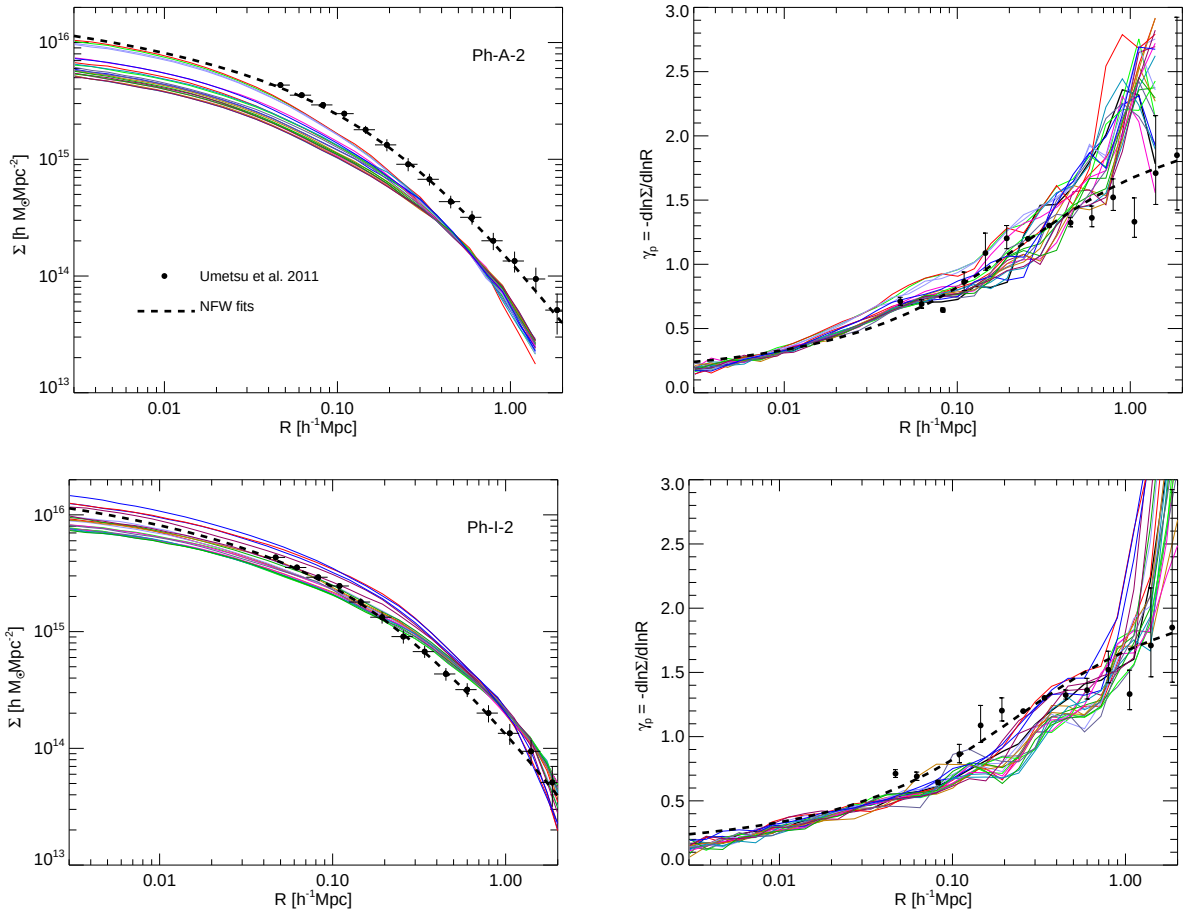

Figure 9. Projected density profiles of Ph-A-2 (top) and Ph-I-2 (bottom). We show 20 different random projections for each cluster. The asphericity of the clusters leads to large variations (up to a factor of 3) in the projected density at a given radius depending on the line of sight. On the other hand, the *shape* of the profile (as measured by the logarithmic slope, $\gamma_p = -d\ln\Sigma/d\ln R$, is much less sensitive to projection effects. Data with error bars correspond to the stacked profile of 4 massive clusters estimated using strong and weak lensing data (Umetsu et al. 2011).

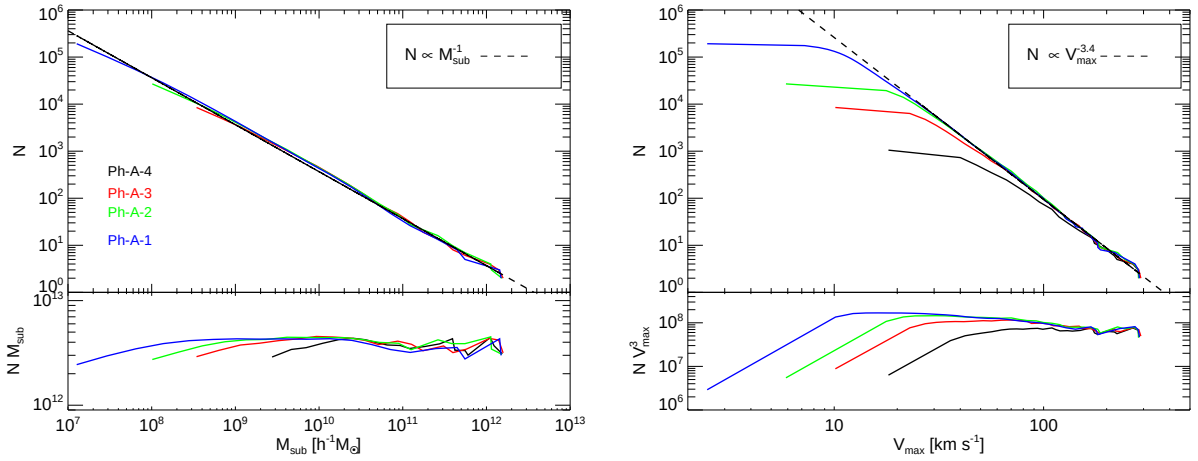

Figure 12. *Left:* The cumulative mass function of substructure haloes ("subhaloes") within the virial radius of cluster Ph-A at $z = 0$. We compare the results of four different realizations of the same halo, Ph-A-1 to Ph-A-4, with varying numerical resolution. The top and bottom panels contain the same information; the bottom shows the number of subhaloes weighted by mass or, equivalently, the fractional contribution of each logarithmic mass bin to the total mass in subhaloes. Each curve extends down to a mass corresponding to 60 particles. Note that, over the range resolved by the simulations, the cumulative function is well approximated by a power-law, $N \propto M^{-1}$, the critical dependence for logarithmically divergent substructure mass. *Right:* Same as left panels, but for the subhalo peak circular velocity.

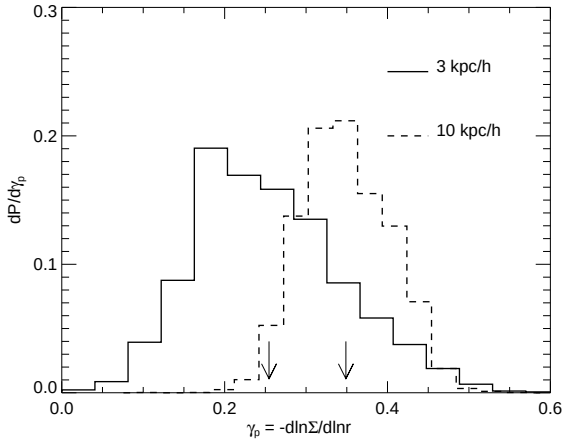

Figure 11. Distribution of the slope of the circularly-averaged surface density profile, $\gamma_p(R)$, measured at two different radii, $R = 3$ and $10\,h^{-1}$ kpc in projection. These histograms are based on 500 random lines of sight for each of the level-2 Phoenix clusters. Vertical arrows show the values corresponding to the projected profile of all nine clusters stacked together. The profiles become gradually shallower towards the centre, but with large scatter: $\langle\gamma_p\rangle$ changes from 0.35 to 0.25 as R goes from 10 to $3\,h^{-1}$ kpc, but the halo-to-halo scatter is quite large, with rms of order 0.09 at $3\,h^{-1}$ kpc and 0.05 at $10\,h^{-1}$ kpc, respectively.

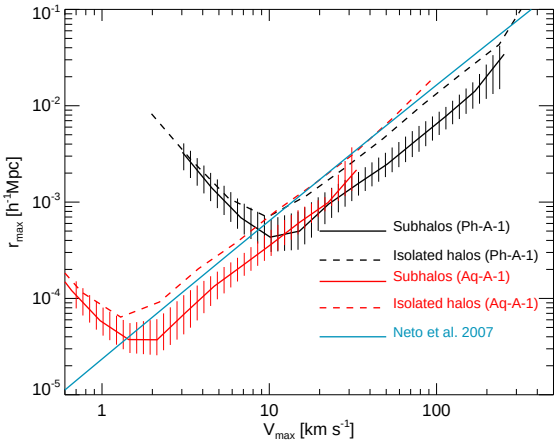

Figure 14. Peak circular velocity, $V_{\rm max}$, vs the radius at which it is reached, $r_{\rm max}$. The solid cyan curve indicates the $r_{\rm max}$-$V_{\rm max}$ relation obtained for isolated haloes in the Millennium Simulation by Neto et al. (2007). Subhaloes in both Phoenix (solid black curve) and Aquarius (solid red curve) deviate systematically from this relation towards smaller $r_{\rm max}$ at a given velocity. This is a result of tidal stripping, which shifts the location of the peak inwards while changing little the peak velocity. Isolated haloes identified in Aquarius and Phoenix (shown with dashed lines) are not subject to tides and are in good agreement with the Millennium Simulation results.

4.1 Mass Function

We start by analyzing the Ph-A simulation series in order to identify the limitations introduced by finite numerical resolution. The top left panel of Fig. 12 shows the cumulative mass function of subhaloes, $N(>M)$, plotted in each case down to the mass corresponding to 60 particles. The bottom left panel shows the same data, but after weighting the numbers by subhalo mass, $M_{\rm sub}$, in order to emphasize the differences between runs. The results show clearly how, as resolution improves, the mass function converges at the low-mass end. Ph-A-4 agrees with higher resolution runs for subhaloes with mass exceeding $\sim 2\times10^{10}\,h^{-1}\,M_\odot$, corresponding to roughly 150 particles; the same applies to Ph-A-3 for mass greater than $\sim 3\times10^{9}\,h^{-1}\,M_\odot$, or ~ 170 particles, and to Ph-A-2 for $\sim 7\times10^{8}\,h^{-1}\,M_\odot$, or 140 particles. We conclude that the subhalo mass function can be robustly determined in Phoenix haloes down to subhaloes containing roughly 150 particles, in good agreement with the results reported for Aquarius haloes (see Fig. 6 of Springel et al. 2008a). For level-2 runs this implies a subhalo mass function that spans over 6 decades in mass below the virial mass of the halo. The subhalo mass function is also routinely expressed in terms of the subhalo peak circular velocity. This is shown in the right-hand panels of Fig. 12 which shows that level-2 Phoenix runs give robust estimates of the abundance of subhaloes down to $V_{\rm max}\sim 20$ km s^{-1}, a factor of ~ 75 lower than the main halo's V_{200}.

Both the subhalo mass and velocity functions seem reasonably well approximated by simple power laws: $N\propto M_{\rm sub}^{-1}$ and $N\propto V_{\rm max}^{-3.4}$, respectively. Interestingly, the M^{-1} dependence corresponds to the critical case where each logarithmic mass bin contributes equally to the total mass in substructure. This is logarithmically divergent as $M_{\rm sub}$ approaches zero, and implies that a significant fraction of the mass could in principle be locked in haloes too small to be resolved by our simulations. We note, however, that even at the resolution of Ph-A-1, of nearly 7 decades in mass, only 8% of the mass within r_{200} is in the form of substructure. Extrapolating down to the Earth mass by assuming that $N\propto M_{\rm sub}^{-1}$, the total mass locked in substructure would still be only about 27 percent.

Fig. 13 compares these results with other level-2 Phoenix clusters in order to assess the general applicability of the Ph-A subhalo mass function. The cumulative number of subhaloes $N(>M)$ is weighted here by $\mu = M_{\rm sub}/M_{200}$ (left panel) in order to emphasize differences as well as to enable the comparison of haloes of different virial mass. Although the subhalo mass function, expressed in this form, is relatively flat in several Phoenix clusters (indicative of an $N\propto M_{\rm sub}^{-1}$ dependence) it is clearly declining in others. The average trend, as indicated by the "stacked" Phoenix cluster (thick dashed black curve) may be approximated, in the range $10^{-6}<\mu<10^{-4}$, by $N\propto\mu^{-0.98}$. This is a slightly steeper dependence than found for Aquarius haloes *over the same mass range*, $N\propto\mu^{-0.94}$ (thick dashed red curve), but still subcritical. The slight difference in the average slope of the Aquarius and Phoenix subhalo mass functions is smaller than the halo-to-halo scatter in either simulation set. This is shown in Table 3, where we list the average parameters of power-law fits of the form,

$$N(>\mu) = N_m\,(\mu/10^{-6})^s, \qquad (4)$$

for Aquarius and Phoenix haloes. The dispersion around $\langle s\rangle$ is similar to the difference between the average slope of Aquarius and Phoenix haloes, suggesting that there is no significant difference in the *shape* of the subhalo mass function of cluster- and Milky-way halo-sized haloes.

Fig. 13 also shows that substructure is slightly more prevalent in clusters than in galaxy-sized haloes. Indeed, at all values of $M_{\rm sub}/M_{200}$ the number of Phoenix subhaloes exceeds that in Aquarius, and this is reflected in the higher values of $\langle N_m\rangle$ (7866 for Phoenix vs 5092 for Aquarius; see Table 3). This is another consequence of the dynamical youth of clusters compared to galaxies (tides take a few orbital times to strip a subhalo), as may be verified by inspection of Table 1: in the cluster that forms latest, Ph-G, sub-

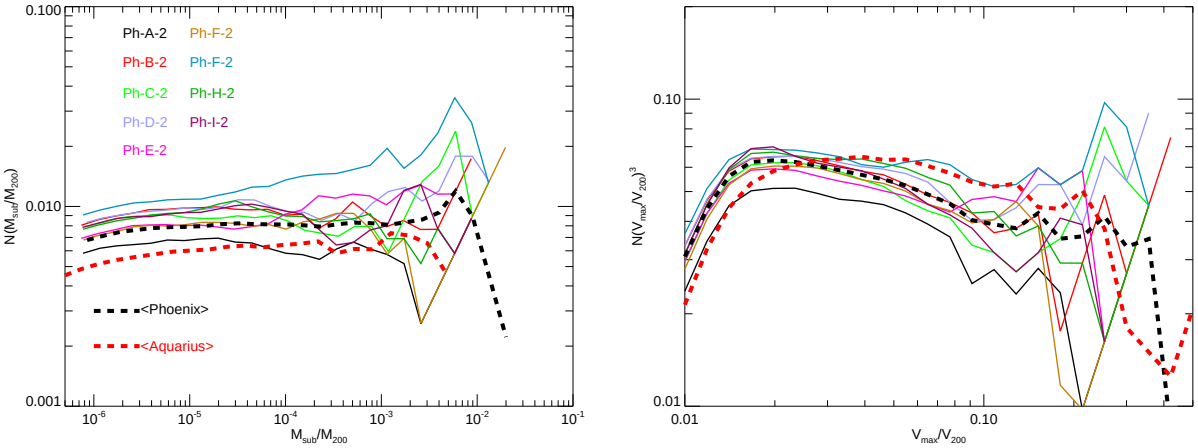

Figure 13. As the bottom panels of Fig. 12, but for all level-2 Phoenix haloes. The cumulative mass function (left panel) is weighted by subhalo mass, expressed in units of the virial mass. A cumulative $N \propto M^{-1}$ dependence, the critical case for logarithmic divergence in the total substructure mass, corresponds to a horizontal curve in these scaled units. Although the dependence is nearly flat in several Phoenix clusters it is clearly declining in others, and the average trend seems to be sub-critical. Compared with Aquarius (thick dashed red curve) the average Phoenix subhalo mass function is slightly steeper. The panel on the right is analogous to the mass function, but for the subhalo peak circular velocity, weighted by $V_{\rm max}^3$. (See text for further discussion.)

structure makes up roughly 17% of its virial mass, but in the earliest collapsing system of the Phoenix series, Ph-A, it makes only 8%.

Interestingly, as a function of $\nu = V_{\rm max}/V_{200}$, the comparison between the Aquarius and Phoenix subhalo functions reverses (right-hand panel of Fig. 13). At a given velocity (scaled to the virial value), subhaloes are more abundant in Aquarius than in Phoenix. This is a consequence of tidal stripping, which affects Aquarius subhaloes more: since tides act to remove preferentially the outer regions of a subhalo, they affect more its mass than its peak circular velocity.

For example, as discussed by Peñarrubia et al. (2008), after losing *half* of its mass to tides, the peak velocity of a subhalo decreases only by $\sim 25\%$. Even after losing 90% of its mass, $V_{\rm max}$ is only reduced by about one half. Since Aquarius haloes form earlier, their subhaloes have been accreted earlier and, on average, have been more stripped than Phoenix subhalos, leading to higher relative velocities for their bound mass than for Phoenix subhalos. This shifts their abundance when measured in terms of peak velocity. In the range $0.025 < \nu < 0.1$ fits to the subhalo function of the form

$$N(>\nu) = N_\nu\,(\nu/0.025)^d \qquad (5)$$

yield $\langle N_\nu \rangle = 4033$ and $\langle d \rangle = -3.13$ for Aquarius and 3984 and -3.32, respectively, for Phoenix (see Table 3). Given the scatter, the difference seems too small to be significant. We conclude that the scaled subhalo velocity function, $N(>\nu)$, is roughly independent of mass (see Wang et al. 2012, for a more thorough discussion of this point).

The effects of tidal stripping on Phoenix subhaloes is shown in Fig. 14. Here we plot $V_{\rm max}$ vs $r_{\rm max}$ for subhaloes identified in Ph-A-1 (solid black curve). This relation is clearly offset from the mean relation that holds for isolated haloes in the Millennium Simulation, as given by Neto et al. (2007) (cyan line). As expected for haloes that have undergone tidal stripping, $r_{\rm max}$ shifts inwards as the subhalo loses mass whilst leaving the peak velocity relatively unchanged (Peñarrubia et al. 2008). Support for this interpretation may be found by inspecting the same relation for "isolated" haloes in Phoenix (i.e., those outside the main halo and that are not embedded in a more massive structure; the $r_{\rm max}$-$V_{\rm max}$ relation for these systems (see dashed lines) is consistent with that of Millennium haloes.

Fig. 14 also includes results for isolated haloes and subhaloes in Aquarius (red lines). The results from the two sets of simulations form a single sequence and this allows us to characterize the structural parameters of subhaloes over a range spanning more than two decades in velocity (and thus over six decades in mass). On average, subhaloes follow the same $r_{\rm max}$-$V_{\rm max}$ scaling relations as isolated haloes, but shifted by about a factor of two in radius (or, alternatively, by $\sim 30\%$ in velocity).

We conclude from this discussion that although substructure does not seem fully invariant with halo mass, the changes are relatively small when comparing the haloes of clusters and galaxies, and depend on whether subhalo masses or velocities are used to characterize substructure. The subhalo mass function of clusters, scaled to halo virial mass, is similar in shape to that of galaxy-sized haloes (which are roughly one thousand times less massive), but with a slightly higher normalization ($\sim 35\%$). The normalization difference disappears when the scaled subhalo velocity function, $N(>\nu)$, is used. The total mass in substructure increases with the dynamical youth of the system and is more prevalent in clusters than on galaxy scales, but only weakly so: the average mass fraction in substructures is 11% for Phoenix and 7% for Aquarius.

4.2 Spatial Distribution

The distribution of subhaloes within the main halo has been the subject of many studies (e.g. Ghigna et al. 2000; Diemand et al. 2004b; De Lucia et al. 2004; Gao et al. 2004b,a; Springel et al. 2008a; Ludlow et al. 2009) over the past decade. This work has demonstrated that substructure does not follow the same spatial distribution as the dark matter: subhaloes tend to populate preferentially the outskirts of the main halo and their spatial distribution is much more extended than the mass. It also hinted that the number density profile of subhaloes is roughly independent of subhalo mass, at least in the subhalo mass range where simulations resolve them well and where they exist in sufficient numbers for their spatial distribution to be determined. This result has been confirmed

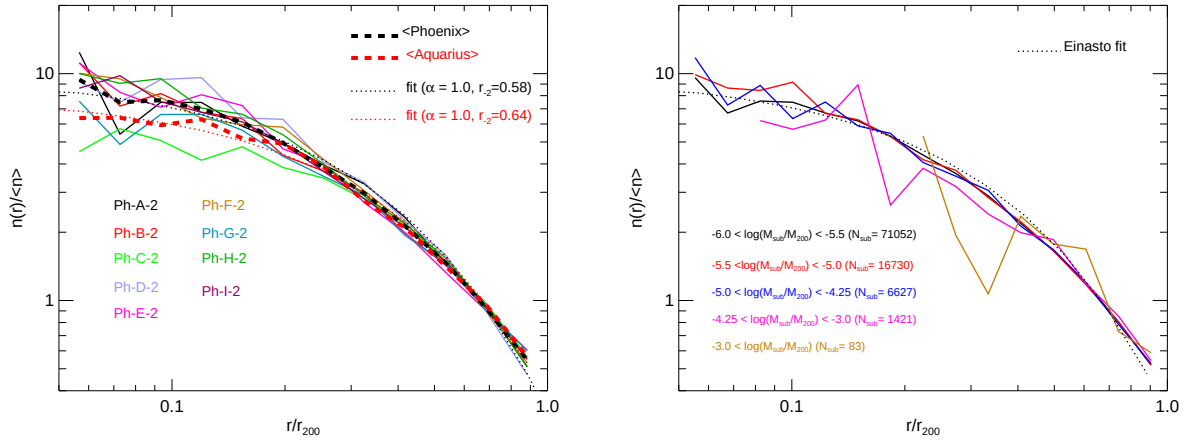

Figure 15. Subhalo number density profiles. The panel on the left shows the spatial distribution of subhaloes with more than 100 particles in each of the 9 Phoenix level-2 clusters. Each profile is normalized to the mean number density of subhaloes within the virial radius. The thick dashed black curve traces the result of stacking all 9 level-2 Phoenix haloes. The profile obtained after stacking all level-2 Aquarius haloes is shown by the red dashed curve. Note that subhaloes are slightly more concentrated in the case of Phoenix than of Aquarius. The panel on the right shows the density profile of subhaloes in different bins of subhalo mass, computed after stacking all 9 level-2 Phoenix clusters. Note that the spatial distribution of subhaloes is approximately independent of subhalo mass.

recently by the Aquarius simulation suite for haloes similar to the Milky Way (Springel et al. 2008a).

A number of observational diagnostics depend on the spatial distribution of substructure, and it is therefore important to verify that this result holds also on galaxy cluster scales. For example, recent analyses indicate that total flux of dark matter annihilation radiation is expected to be dominated by low-mass subhaloes (Kuhlen et al. 2008; Springel et al. 2008b; Gao et al. 2011b). It is therefore crucial to constrain their spatial distribution in order to understand the expected angular distribution of the annihilation flux and to design optimal filters to aid its discovery (see, e.g., Pinzke et al. 2011; Gao et al. 2011b).

We show the number density profile of subhaloes in Fig. 15. The left panel shows the profiles for each of the 9 level-2 Phoenix haloes (thin lines), as well as the profile corresponding to stacking all 9 haloes after scaling them to the virial mass and radius of each cluster (thick dashed black curve). All subhaloes with more than 100 particles have been used for this plot. This figure clearly confirms the results of earlier work: the subhalo distribution is more extended than that of the dark matter; In addition there is a well defined "core" in the central density of the subhalo distribution; Subhaloes primarily populate the outskirts of the main halo.

There is also considerable halo-to-halo scatter, especially near the centre, where the number density of subhaloes may vary by up to a factor of three. Comparing the average number density profile of Phoenix with that of Aquarius (thick red dashed curve) reveals that cluster subhaloes are slightly more abundant near the centre, by up to 50% at $r = 0.1 r_{200}$. In the outskirts of the main halo both Aquarius and Phoenix give similar results. As discussed by Ludlow et al. (2009), the number density profile can be fitted accurately by an Einasto profile (eq. 7), just like the dark matter, but with quite different shape parameters: $\alpha \sim 1$ for subhaloes but ~ 0.2 for the main halo. An Einasto fit to the Phoenix subhalo profile yields $r_{-2} = 0.58 r_{200}$ and $\alpha = 1.0$. For Aquarius, the same procedure yields $r_{-2} = 0.64 r_{200}$ and $\alpha = 1.0$, and a central density normalization lower by a factor of 1.3, when expressed in units of $\langle n \rangle$, the mean number density of subhaloes within r_{200}.

Simplified schemes for populating dark matter simulations

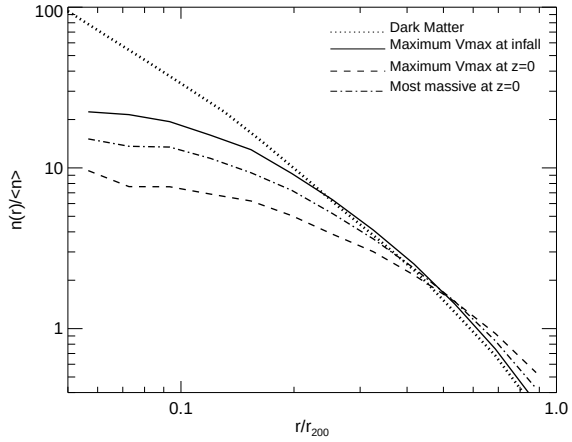

Figure 16. Stacked subhalo number density profiles as a function of r/r_{200} for the nine Phoenix haloes and for different definitions of the lower subhalo "mass" limit. The solid line shows the radial profile for all subhaloes whose progenitors had a maximum circular $V_{\rm max}$ exceeding 45 km s^{-1} when they first fell into the cluster; the dot-dashed line shows a similar profile but for subhaloes with $V_{\rm max}$ greater than 30 km s^{-1} at the present day; finally, the dashed line show the profile for all subhaloes containing more than 200 bound particles. For comparison, a dotted line shows the stacked dark matter mass profile of the clusters. The profiles are normalised to integrate to the same value within r_{200}. Note that none of the subhalo profiles matches the shape of the dark matter profile within $0.25 r_{200}$.

with galaxies make a variety of assumptions about how to assign galaxies to subhaloes. A number of authors have argued that although present subhalo mass and maximum circular velocity are strongly affected by tidal stripping and so are poor indicators of galaxy properties, the mass or circular velocity at infall are plausibly much better and give meaningful results when used in subhalo abundance matching analyses (Vale & Ostriker 2004; Conroy et al. 2006; Behroozi et al. 2010; Guo et al. 2010). We study this issue in Fig. 16, which shows stacked number density profiles for subhalo

samples defined above thresholds in present mass, present circular velocity and infall circular velocity. Note that these thresholds are chosen so that each sample contains roughly 6000 subhaloes. In agreement with earlier work, we see that sample definition has a substantial effect on the inferred radial profile of the subhalo population. Subhalo samples defined by present mass have shallower profiles than samples defined by present circular velocity which, in turn, have shallower profiles than samples defined by infall circular velocity. Note, however, that all these profiles differ substantially from the mean dark matter density profile, especially in the inner regions ($r < 0.25\,r_{200}$), whereas observations show the mean galaxy number density profiles in the inner regions of clusters to follow the mean dark matter profiles quite closely (e.g. Carlberg et al. 1997; Biviano & Girardi 2003; Sheldon et al. 2009). Semi-analytic models which explicitly follow the formation of galaxies within the evolving subhalo population provide a better match to the observed inner profiles because they include a population of "orphan" galaxies whose dark matter subhaloes have already been tidally destroyed (Gao et al. 2004a; Wang et al. 2006; Guo et al. 2011).

Fig. 17 shows the fractional contribution of substructure to the total mass of the halo, as a function of radius, either in cumulative (left panel) or differential (right panel) form. This figure shows quantitatively that substructure contributes only a small fraction of the halo mass. This contribution peaks in the outer regions; it is only 0.1% at $r = 0.02\,r_{200}$ but it reaches 10-20% at the virial radius. The total mass contribution is, on average, just over 10% (see also Table 2). Results for Phoenix are similar to Aquarius, adjusted up by a modest amount that reflects the overall larger substructure fraction present in clusters relative to galaxy-sized haloes. This adjustment is mainly noticeable in the inner regions, reflecting our earlier conclusion that substructure in Phoenix is more centrally concentrated than in Aquarius.

5 SUMMARY AND CONCLUSIONS

We present the Phoenix Project, a series of simulations of the formation of rich galaxy cluster halos in the ΛCDM cosmogony. Phoenix simulations follow the dark matter component of 9 different clusters with numerical resolution comparable to that of the Milky Way-sized haloes targeted in the Aquarius Project (Springel et al. 2008a; Navarro et al. 2010). We report here on the basic structural properties of the simulated clusters and their substructure, and compare them with those of Aquarius haloes in order to highlight the near mass invariance of cold dark matter haloes in the absence of baryonic effects. Our main results may be summarized as follows.

`Radial Profiles.` The recent formation of galaxy clusters causes many of them to be rapidly evolving and unrelaxed. This results in mass profiles that are less well approximated by simple fitting formulae such as the NFW or Einasto profiles than those of galaxy haloes. Stacking clusters helps to average out inhomogeneities in the mass distribution characteristic of transient states. The mass profile of the stacked cluster is very similar to that of Aquarius haloes; it can be well approximated by an Einasto profile, albeit with a slightly larger value of the shape parameter, α, and significantly lower concentration. The similarity extends to the dynamical properties of the haloes: when properly scaled, the average pseudo-phase-space density and velocity anisotropy profiles of Aquarius and Phoenix haloes are indistinguishable.

`Density Cusp.` The central density cusp has, at the innermost resolved radius ($r_{\rm conv} \sim 2\times10^{-3}\,r_{200}$), an average logarithmic slope $\langle\gamma\rangle = 1.05 \pm 0.19$, where the "error" refers to the halo-to-halo rms dispersion of the 9 level-2 Phoenix runs. This is only slightly steeper than that of Aquarius haloes at comparable radii, for which $\langle\gamma\rangle = 1.01 \pm 0.10$). Although in some clusters γ remains roughly constant over a sizeable radial range near the centre, in the majority of cases the profile keeps getting shallower all the way to the innermost converged radius, with little evidence of convergence to an asymptotic power-law behaviour.

`Projected Profiles.` Because of their aspherical nature, the surface density of Phoenix haloes varies greatly depending on the line of sight, in some cases by up to a factor of ~ 3 at a given projected radius. This affects especially the inner regions and may give rise to substantially biased estimates of a cluster's total mass and concentration. For example, NFW fits to the inner $500\,h^{-1}$ kpc of 9 Phoenix haloes, on average, lead to estimates of M_{200} and c that can be overestimated by 20% and 80%, respectively, when the cluster is projected along the major axis and underestimated by 30% and 20% respectively when seen along the minor axis. The *shape* of the surface density profile, on the other hand, is hardly affected by projection. The average logarithmic slope of the surface density profile declines gradually towards the centre, from $\langle\gamma_p\rangle = 0.35 \pm 0.091$ at $R = 10\,h^{-1}$ kpc to 0.21 ± 0.054 at $R = 3\,h^{-1}$ kpc, again with no clear sign of approaching a power-law asymptotic behaviour.

`Substructure Mass Function.` Substructure is more abundant (by about $\sim 35\%$ on average) in Phoenix clusters than in galaxy haloes. At a given $\mu = M_{\rm sub}/M_{200}$, the cumulative number of cluster subhaloes is higher in Phoenix by about $\sim 30\%$ compared to Aquarius, with a tendency for the excess to increase at the low-mass end. In some cases the subhalo mass function is best approximated by a power law with the critical slope $N \propto \mu^{-1}$. There is significant halo-to-halo scatter, however, and the average trend is subcritical. In the range $1\times10^{-6} < \mu < 1\times10^{-4}$ we find that $N = 0.010\,\mu^{-0.98}$ fits well the composite subhalo mass function of the 9 level-2 Phoenix clusters stacked together. For comparison, the same procedure for the Aquarius haloes yields a very similar result: $N = 0.012\,\mu^{-0.94}$.

`Substructure Spatial Distribution.` We confirm earlier reports that subhaloes are biased tracers of the halo mass distribution, avoiding the central regions and increasing in prevalence gradually from the centre outwards. As in galaxy haloes, the subhalo number density profile appears to be independent of subhalo mass, and may be approximated accurately by an Einasto profile, but with scale radius $\sim 0.58\,r_{200}$ and a shape parameter much greater than that of the dark matter distribution, $\alpha \sim 1.0$. Phoenix subhaloes are slightly more concentrated than those of Aquarius haloes: inside $0.1\,r_{200}$ they make up roughly 0.05% of the enclosed mass, a factor of 2 to 3 times larger than in Aquarius haloes. The difference decreases with increasing radius; in total Phoenix subhaloes make up on average 11% of the total mass, compared with 7% for Aquarius.

Our analysis confirms the remarkable structural similarity of CDM haloes of different mass, whilst at the same time emphasizing the small but systematic differences that arise as halo mass increases from galaxies to clusters. Many of these differences may be ascribed to the dynamical youth of galaxy clusters, which lead to larger deviations of individual clusters from the average trends. This argues for combining the results of as many clusters as possible in order to average over the transient features of individual systems and to uncover robust trends that may be fruitfully compared with the predictions of the ΛCDM paradigm.

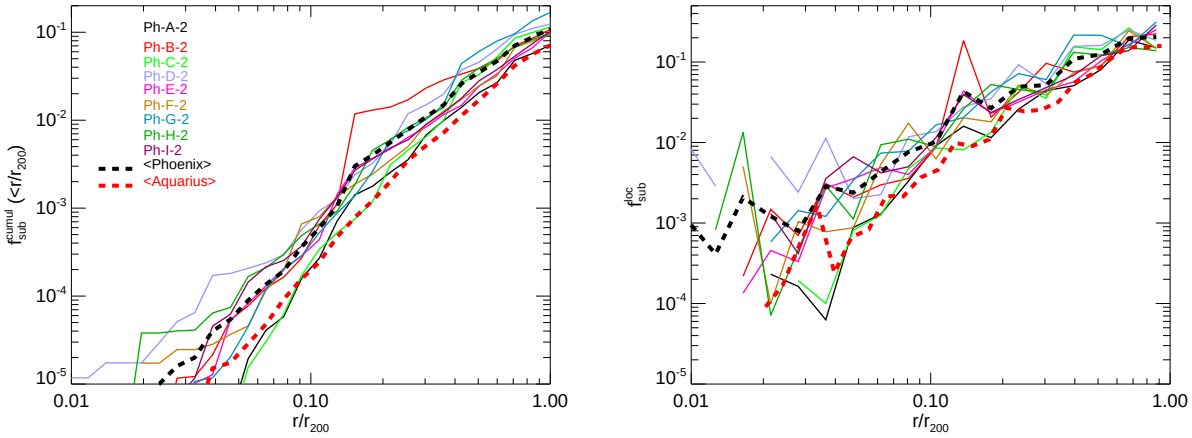

Figure 17. *Left panel*: Cumulative fractional contribution of subhaloes (resolved with more than 100 particles) to the enclosed mass, shown as a function of radius for all level-2 Phoenix clusters (thin lines). A thick dashed black curve shows the average trend, computed after stacking all 9 Phoenix haloes. The corresponding result for Aquarius is shown by the thick dashed red curve. *Right panel*: Fraction of total mass contributed by substructure in different radial bins. As in the left panel, only subhaloes with more than 100 particles are considered; black and red thick dashed lines correspond to the average trend computed after stacking all level-2 Phoenix and Aquarius haloes, respectively.

ACKNOWLEDGEMENTS

Phoenix is a project of the Virgo Consortium. Most simulations were carried out on the Lenova Deepcomp7000 supercomputer of the super Computing Center of Chinese Academy of Sciences, Beijing, China, and on Cosmology machine at the Institute for Computational Cosmology (ICC) at Durham. The Cosmology machine is part of the DiRAC facility jointly founded by STFC, the large facilities capital fund of BIS, and Durham University. LG acknowledges support from the one-hundred-talents program of the Chinese academy of science (CAS), the National Basic Research Program of China (program 973 under grant No. 2009CB24901), NSFC grants (Nos. 10973018 and 11133003), MPG partner Group family, and an STFC Advanced Fellowship, as well as the hospitality of the Institute for Computational Cosmology at Durham University. CSF acknowledges a Royal Society Wolfson Research Merit Award and ERC Advanced Investigator grant, COSMIWAY. This work was supported in part by an STFC rolling grant to the ICC. We thank the anonymous referee for a thoughtful and useful report.

REFERENCES

Behroozi P. S., Conroy C., Wechsler R. H., 2010, ApJ, 717, 379
Bertschinger E., 1985, ApJS, 58, 39
Biviano A., Girardi M., 2003, ApJ, 585, 205
Buote D. A., Gastaldello F., Humphrey P. J., et al., 2007, ApJ, 664, 123
Carlberg R. G., Yee H. K. C., Ellingson E., et al., 1997, ApjL, 485, L13
Conroy C., Wechsler R. H., Kravtsov A. V., 2006, ApJ, 647, 201
Corless V. L., King L. J., 2007, MNRAS, 380, 149
Davis M., Efstathiou G., Frenk C. S., White S. D. M., 1985, ApJ, 292, 371
De Lucia G., Kauffmann G., Springel V., et al., 2004, MNRAS, 348, 333
Diemand J., Kuhlen M., Madau P., 2007, ApJ, 657, 262
Diemand J., Moore B., Stadel J., 2004a, MNRAS, 353, 624
Diemand J., Moore B., Stadel J., 2004b, MNRAS, 352, 535
Einasto J., 1965, Trudy Inst. Astroz. Alma-Ata, 51, 87
Frenk C. S., White S. D. M., Efstathiou G., Davis M., 1985, Nat, 317, 595
Gao L., De Lucia G., White S. D. M., Jenkins A., 2004a, MNRAS, 352, L1
Gao L., Frenk C. S., Boylan-Kolchin M., Jenkins A., Springel V., White S. D. M., 2011a, MNRAS, 410, 2309
Gao L., Frenk C. S., Jenkins A., Springel V., White S. D. M., 2011b, ArXiv e-prints
Gao L., Navarro J. F., Cole S., et al., 2008, MNRAS, 387, 536
Gao L., White S. D. M., Jenkins A., Stoehr F., Springel V., 2004b, MNRAS, 355, 819
Ghigna S., Moore B., Governato F., Lake G., Quinn T., Stadel J., 2000, ApJ, 544, 616
Gralla M. B., Sharon K., Gladders M. D., et al., 2011, ApJ, 737, 74
Guo Q., White S., Boylan-Kolchin M., et al., 2011, MNRAS, 413, 101
Guo Q., White S., Li C., Boylan-Kolchin M., 2010, MNRAS, 404, 1111
Jenkins A., 2010, MNRAS, 403, 1859
Jenkins A., Frenk C. S., Pearce F. R., et al., 1998, ApJ, 499, 20
Jing Y. P., Suto Y., 2000, ApjL, 529, L69
Jing Y. P., Suto Y., 2002, ApJ, 574, 538
Komatsu E., Smith K. M., Dunkley J., et al., 2011, ApJS, 192, 18
Kuhlen M., Diemand J., Madau P., 2008, ApJ, 686, 262
Ludlow A. D., Navarro J. F., Springel V., et al., 2010, MNRAS, 406, 137
Ludlow A. D., Navarro J. F., Springel V., Jenkins A., Frenk C. S., Helmi A., 2009, ApJ, 692, 931
Mao S., Jing Y., Ostriker J. P., Weller J., 2004, ApjL, 604, L5
Mao S., Schneider P., 1998, MNRAS, 295, 587
Meneghetti M., Bartelmann M., Jenkins A., Frenk C., 2007, MNRAS, 381, 171
Moore B., Quinn T., Governato F., Stadel J., Lake G., 1999, MNRAS, 310, 1147
Natarajan P., De Lucia G., Springel V., 2007, MNRAS, 376, 180

Natarajan P., Kneib J.-P., Smail I., et al., 2009, ApJ, 693, 970
Navarro J. F., Frenk C. S., White S. D. M., 1996, ApJ, 462, 563
Navarro J. F., Frenk C. S., White S. D. M., 1997, ApJ, 490, 493
Navarro J. F., Hayashi E., Power C., et al., 2004, MNRAS, 349, 1039
Navarro J. F., Ludlow A., Springel V., et al., 2010, MNRAS, 402, 21
Neto A. F., Gao L., Bett P., et al., 2007, MNRAS, 381, 1450
Newman A. B., Treu T., Ellis R. S., et al., 2009, ApJ, 706, 1078
Oguri M., Bayliss M. B., Dahle H., et al., 2011, ArXiv e-prints
Oguri M., Takada M., Okabe N., Smith G. P., 2010, MNRAS, 405, 2215
Okabe N., Takada M., Umetsu K., Futamase T., Smith G. P., 2010, PASJ, 62, 811
Peñarrubia J., Navarro J. F., McConnachie A. W., 2008, ApJ, 673, 226
Pinzke A., Pfrommer C., Bergstrom L., 2011, ArXiv e-prints
Postman M., Coe D., Benitez N., et al., 2011, ArXiv e-prints
Power C., Navarro J. F., Jenkins A., et al., 2003, MNRAS, 338, 14
Reed D., Governato F., Verde L., et al., 2005, MNRAS, 357, 82
Sand D. J., Treu T., Ellis R. S., 2002, ApjL, 574, L129
Sand D. J., Treu T., Smith G. P., Ellis R. S., 2004, ApJ, 604, 88
Sereno M., Jetzer P., Lubini M., 2010, MNRAS, 403, 2077
Sheldon E. S., Johnston D. E., Masjedi M., et al., 2009, ApJ, 703, 2232
Springel V., Frenk C. S., White S. D. M., 2006, Nat, 440, 1137
Springel V., Wang J., Vogelsberger M., et al., 2008a, MNRAS, 391, 1685
Springel V., White S. D. M., Frenk C. S., et al., 2008b, Nat, 456, 73
Springel V., White S. D. M., Jenkins A., et al., 2005, Nat, 435, 629
Springel V., White S. D. M., Tormen G., Kauffmann G., 2001a, MNRAS, 328, 726
Springel V., Yoshida N., White S. D. M., 2001b, New Astronomy, 6, 79
Stadel J., Potter D., Moore B., et al., 2009, MNRAS, 398, L21
Taylor J. E., Navarro J. F., 2001, ApJ, 563, 483
Umetsu K., Broadhurst T., Zitrin A., Medezinski E., Coe D., Postman M., 2011, ApJ, 738, 41
Vale A., Ostriker J. P., 2004, MNRAS, 353, 189
Wang J., Frenk C. S., Navarro J. F., Gao L., 2012, ArXiv e-prints
Wang J., Navarro J. F., Frenk C. S., et al., 2011, MNRAS, 413, 1373
Wang L., Li C., Kauffmann G., De Lucia G., 2006, MNRAS, 371, 537
Xu D. D., Mao S., Wang J., et al., 2009, MNRAS, 398, 1235
Zitrin A., Broadhurst T., Coe D., et al., 2011, ArXiv e-prints

6 APPENDIX

6.1 Fitting formulae

The fitting formulae used to describe the mass profile of Phoenix haloes are the following: (i) The NFW profile (Navarro et al. 1996, 1997), given by

$$\rho(r) = \frac{\rho_s}{(r/r_s)(1+r/r_s)^2}, \tag{6}$$

and (ii) the Einasto profile (Einasto 1965),

$$\ln(\rho(r)/\rho_{-2}) = (-2/\alpha)[(r/r_{-2})^\alpha - 1]. \tag{7}$$

Because these formulae define the characteristic parameters in a slightly different way, we choose to reparametrise them in terms of r_{-2} and $\rho_{-2} \equiv \rho(r_{-2})$, which identify the "peak" of the $r^2\rho$ profile shown in the left panel of Fig. 4. This marks the radius where the logarithmic slope of the profile, $\gamma(r) = -d\ln\rho/d\ln r$, equals the isothermal value, $\gamma = 2$. We note that, unlike NFW, when α is allowed to vary freely the Einasto profile is a 3-parameter fitting formula.

6.2 Fitting procedure

We compute the density profiles of each halo in 32 radial bins equally spaced in $\log_{10} r$, in the range $r_{\rm conv} < r < r_{200}$. All haloes are centred at the minimum of the gravitational potential. Best-fit parameters are found by minimizing the deviation between model and simulation across all bins in a specified radial range. In the case of the density profile, the best fit is found by minimizing the figure-of-merit function, Q^2, defined by

$$Q^2 = \frac{1}{N_{\rm bins}} \sum_{i=1}^{N_{\rm bins}} (\ln\rho_i - \ln\rho_i^{\rm model})^2. \tag{8}$$

This function provides a simple measure of the level of disagreement between simulated and model profiles. It is dimensionless; it weights different radii logarithmically; and, for a given radial range, Q^2 is roughly independent of the number of bins used in the profile. The actual value of Q is thus a reliable and objective measure of the average per-bin deviation from a particular model. Thus, minimizing Q^2 yields for each halo well-defined estimates of a model's best-fit parameters. The values of $Q_{\rm min}$ for each halo are given in Table 2 for both Einasto and NFW fits.

It is less clear how to define a goodness-of-fit measure associated with Q^2 and, consequently, how to assign statistically-meaningful confidence intervals to the best-fit parameter values. We have explored this issue in Navarro et al. (2010) and we refer the interested reader to that paper for details.